12-14-2016

# Investigating the Effect of Aluminum Substitution on the Physical and Chemical Properties of Ferrihydrite

Richard Ajewole

# INVESTIGATING THE EFFECT OF ALUMINUM SUBSTITUTION ON THE PHYSICAL AND CHEMICAL PROPERTIES OF FERRIHYDRITE

By

RICHARD AJEWOLE

Under the Direction of Nadine Kabengi, PhD

## ABSTRACT

This thesis investigated the impact of aluminum (Al) substitution in ferrihydrite (FH) on both its chemical and physical properties. Al was coprecipitated with FH under controlled hydrolysis conditions to yield various % mol substitutions. Sulfate adsorption was measured across pHs to examine any changes in surface reactivity. The samples' morphology, specific surface areas (SSAs), crystallinity, and phase transformation upon heating were evaluated and parameterized to allow conclusions on the role of Al on the physical properties. Sulfate sorption diminished across pHs for all Al saturation levels. X-ray Diffraction revealed goethite (GT) presence was negatively influenced by Al. The SSAs of samples increased non-linearly with increasing % mol Al, indicating a decreasing particle size with more Al content. Transmission Electron Microscopy micrographs showed the FH nanoparticles transformed to acicular/blocky laths of GT crystals and lenticular/platy hematite (HM) crystals with occasional grainy appearance at both room temperature and upon active heating. The phase transformation alongside the derived aspect ratios (length/width) of the GT crystals were retarded by the Al substitution.

INDEX WORDS: Ferrihydrite, Oxyhydroxide, Adsorption, Co-precipitation, Aluminum, Sulfate, Speciation, Sorbent, XRD, Spectroscopy, Morphology

# INVESTIGATING THE EFFECT OF ALUMINUM SUBSTITUTION ON THE PHYSICAL AND CHEMICAL PROPERTIES OF FERRIHYDRITE

by

RICHARD AJEWOLE

A Thesis Submitted in Partial Fulfillment of the Requirements for the Degree of

Master of Science

in the College of Arts and Sciences

Georgia State University

2016

# INVESTIGATING THE EFFECT OF ALUMINUM SUBSTITUTION ON THE PHYSICAL AND CHEMICAL PROPERTIES OF FERRIHYDRITE

by

RICHARD AJEWOLE

Committee Chair: Nadine Kabengi

Committee: Daniel Deocampo

Maria Chrysochoou

Electronic Version Approved:

Office of Graduate Studies

College of Arts and Sciences

Georgia State University

December 2016

## DEDICATION

I would like to dedicate this thesis to my parents for always urging me on to relentlessly pursue my dreams and prayerfully supporting me through all these years. I also would like to thank my dear friends and family relatives for the unwavering financial and moral support shown towards my physical and mental wellbeing.

## ACKNOWLEDGEMENTS

I would like to acknowledge Georgia State University and the Department of Geosciences for providing the avenue for me to partake in immersive learning experiences that give the requisite skills and knowledge for academic research and gainful employment.

I also would like to thank Dr. Deocampo for serving on my committee, offering academic counseling when I seriously needed one, and making insightful suggestions on how to obtain XRD data for my samples.

My unreserved appreciation also goes to Dr. Maria Chrysochoou; another member on my defense committee, whose many findings on the surface structure and reactivity of Aluminum-substituted Ferrihydrite aided the understanding of my experimental results.

Not to be forgotten is my Thesis Advisor, Dr. Kabengi, who trusted in my intellectual capability to produce this work. She guided and supported me throughout the experimental work for this thesis, and her inputs in interpreting and writing the results were top-notch. I also enjoyed contribution from her research team comprising prospective Ph.D. candidate, Nick Allen; who helped with HPLC analysis, David Davis; who assisted me during the centrifugation of my samples and preparation for XRD analysis, Tyler Hawkins; who was consistently available whenever I needed clarification on an experimental process.

Special thanks to Dr. Emily Beverly for helping to run my samples on the X-ray diffractometer and showing me how to overlay several diffractograms on same axes.

Finally, I would like to acknowledge support by the Virginia Tech National Center for Earth and Environmental Nanotechnology Infrastructure (NanoEarth), a member of the National Nanotechnology Coordinated Infrastructure (NNCI), funded by NSF (ECCS 1542100). TEM, SEM, and Specific Surface Area through BET analyses were performed at this research facility.

Mrs. Deborah Berti; a research associate at the facility, helped with the collection of both TEM and SEM micrographs and also showed me how to obtain qualitative and quantitative information from the micrographs.

# TABLE OF CONTENTS

# LIST OF TABLES

# LIST OF FIGURES

# 1 INTRODUCTION

## 1.1 Ferrihydrite Occurrence and Description

Ferrihydrite (FH) is a ferric oxyhydroxide found pervasive in various Earth surface systems, mostly occurring at the nanoscale. Naturally, FH forms in the presence of compounds with strong affinity for Fe oxide surface (Sposito, 1989). For instance, FH is found prevalent in soils where Fe(II) is abiotically oxidized, and the mineral formed consequently coprecipitated with, or adsorbed by soluble silicate or organic anions found in the soils thereby inhibiting the formation of more crystalline iron oxides: hematite and goethite (Childs, 1992). Other types of environments where FH is found locally include the following: freshwater and marine systems, areas impacted by mining such as acid mine drainage (AMD) environments, aquifers with high levels of ferriferous groundwater, hydrothermal hot springs, and ocean floor where the oxide is found in association with Mn oxides and occurs mostly as nodules (Sullivan and Bush, 2004; Adra et al., 2013; Cheng et al., 2011; Pham et al., 2012; Hrischeva and Scott, 2007).

On the other hand, synthetic FH according to Schwertmann and Cornell (2000), can be formed by the rapid oxidation of aqueous Fe(II) under normal ambient conditions. FH can also be synthesized in the laboratory by direct precipitation as the first mineral phase from oxygenated iron-rich aqueous solutions (Alarcón et al., 2014).

## 1.2 Crystal Structure of Ferrihydrite and Latest Findings

Structurally, FH exhibits short-range structural order, giving it a poor crystallinity and a nanoparticulate character (Cismasu et al., 2011). In FH most disordered state, powder X-ray diffraction pattern reveals two broad X-ray diffraction (XRD) peaks. In its most crystalline state, a maximum of six strong lines are however observed (Schwertmann, 1988). Therefore, using the

size of FH constitutive crystallites as the basis of differentiation between the two diffraction end members, FH is named accordingly as two-line (2LFH) or six-line FH (6LFH) (Childs, 1992; Drits et al., 1993).

FH also shows marked compositional variations due to its variable water content and lack of a known crystal structure (Cismasu et al., 2011). As a consequence, different formulae have been proposed for FH: $5Fe_2O_3.9H_2O$ (Fleischer et al., 1975), $Fe_5HO_8.\ 4H_2O$ (Towe and Bradley, 1967), and $Fe_2O_3.2FeOOH.2.6H_2O$ (Rusell, 1979).

According to the International Mineralogical Association (IMA), the general adopted FH structural model has a trigonal unit cell (a = 5.08 Å and c = 9.4 Å) derived from hexagonal-close-packed layers of $O_2$, OH, $H_2O$ with Fe(III) coordinated in octahedral positions (Parfitt et al., 1992). However, the octahedral coordination of Fe(III) has been proposed to be limited to the mineral core while the surface of FH referred to as the "inter-phase" has Fe in tetrahedral coordination (Jambor and Dutrizac, 1998). These authors attributed FH high adsorptive capacity to be responsible for its "coordination unsaturated" surface sites.

X-ray spectroscopic studies have also shown FH structure to have close similarities to FeOOH-type minerals such as goethite and akaganeite (Jambor and Dutrizac, 1998). However, the complexity of FH structure makes it a continuous research area as a proper view of its surface structure offers insight into its ion adsorption behavior (Childs, 1992).

Hence, to understand mineral phase stability of Fe oxides in nature (Navrotsky et al., 2008) and biogeochemical activities such as the disintegration of greenhouse gases (Beal et al., 2009), an analysis on FH composition is highly pertinent. Michel et al. (2007) synthesized FH samples at three distinct average coherent scattering domain sizes of approximately 2nm, 3nm, and 6nm. Pair Distribution Function (PDF) analysis of X-ray total scattering data was applied to the samples to

perform structural analysis. The generated result showed the structure of the samples to appear to be single phase contradicting the long posited multiple phase structure model. Maillot et al. (2011) suggested a model that includes tetrahedrally coordinated Fe(III) based on extended X-ray absorption fine structure (EXAFS) analysis performed on a large batch of synthetic FH. Hiemstra and Van Riemsdijk (2009) and Hiemstra (2013) developed a surface structural model for FH by exploring the effects of surface structure and composition of FH nanoparticles on ion-binding and surface charge development. Properties such as mass density, molar mass, specific surface area (SSA), particle size, and site densities of numerous reactive surface groups, were quantified and tabulated.

### 1.3 Charge/Surface Properties of Ferrihydrite

Alongside structure and composition, understanding the surface properties of FH nanoparticles gives an insight into their surface reactivity and interaction with different aqueous species (Cismasu et al., 2012). For instance, FH has a high point-of-zero-charge (PZC), making it positively charged over most soil pH ranges (Spadini et al., 2003; Hofmann et al., 2005; Gilbert et al., 2007, 2009; Nagata et al., 2009; Antelo et al., 2010). These authors have also reported the PZC of FH to be between 7.9 and 8.1 for fresh, and not rigorously de-carbonated FH samples, and between 8.6 and 8.7 for dialyzed and $N_2$-purged samples after synthesis. Cismasu et al. (2013) found the PZC of aluminous FH (ALSFH) to increase from 8.5 to 9 with increasing Al content from 0 to 20 % Al.

FH as a common hydrous ferric oxide nanomineral has small particle sizes (1.5 – 5 nm) giving it a high surface area (>200 $m^2g^{-1}$) at the mineral/water interface (Villalobos & Antelo,

2011). Davis and Leckie (1978) and Dzombak and Morel (1990) also reported the surface area of FH to be as high as ~600 $m^2/g$.

The surface of FH is also densely occupied by amphoteric functional groups that participate in both charge development and ligand exchange reactions (Johnston & Chrysochoou, 2016).

## 1.4 Characterization Techniques for Ferrihydrite

Given that FH affects the mobility of nutrients, trace elements, and contaminants in aquatic and terrestrial environments, it is important to characterize its different properties as a vital mineral sorbent (Cismasu et al., 2011, 2012). The methods often adopted in describing both physical and chemical properties of FH include chemical composition by acid digestion, X-ray diffraction (XRD), specific surface area determination through Brunauer-Emmett-Teller (BET) analysis, Transmission Electron Microscopy (TEM) combined with Energy Dispersive X-ray Spectroscopy (EDXS), Scanning Electron Microscopy (SEM), adsorption edges, and many chemical and physical techniques. (Schwertmann & Cornell, 2008). These methods have enabled an in-depth understanding of the morphology and sorption behavior of FH thereby allowing research to focus extensively on FH as a crucial sequester of harmful oxyanions such as sulfate, chromate, arsenate, vanadate, phosphate, etc., in both natural (contaminated waters) and industrial systems (Yoko Masue, Richard H. Loeppert, & Kramer, 2007; Adra et al., 2013; Wijnja & Schulthess, 2002; Swedlund, Webster, & Miskelly, 2009; Naeem, Westerhoff, & Mustafa, 2007).

## 1.5 Common Ionic Substitutions in Ferrihydrite

FH is rarely pure in natural systems, and often contains a significant amount of impurity such as Silicon (Si) which may be either partly polymerized or bonded via Si-O-Fe bonds (Carlson

and Schwertmann, 1981). Additionally, FH often coexists with structural impurities such as $Al^{III}$, $Mn^{III}$, $Cr^{III}$, $V^{III}$ which infiltrated the structure through isomorphous substitution; the presence of these impurities greatly influences FH retention of environmental contaminants as well as its potential application in water treatment processes (Adra et al., 2013). According to Cornell and Schwertmann (2003), Al is the most invasive substituent in natural and synthetic Fe oxides. Some previous studies that have been conducted on the incorporation of Al into FH structure by different researchers are summarized below.

Cismasu et al. (2012) investigated the effects of Al contents (between 5-40 %) and precipitation rates (rapid and slow) on the structure of 2LFH. They employed a variety of laboratory (TEM, Nuclear Magnetic Resonance (NMR), Inductively Coupled Plasma Atomic Emission Spectroscopy (ICP-AES)) and synchrotron-based techniques (X-ray total scattering and PDF, scanning transmission X-ray microscopy, Al K-edge X-ray absorption near edge structure spectroscopy (XANES)) to study the crystallinity, phase purity, and Al speciation in the FH nanoparticles. Two ALSFH series were prepared by co-precipitation from Al and Fe nitrate solutions under controlled hydrolysis conditions. Their results revealed that Al interacted with the FH structure via octahedral coordination and substituted for Fe in the structure by 20-30% regardless of the method of synthesis adopted. Beyond 30% Al substitution, separate aluminous phases (gibbsite) were observed in the samples that were slowly precipitated. However, NMR spectroscopy also detected phase separation in samples with lower Al content (particularly those slowly precipitated) even though this was below the detection limit of the XRD analysis carried out on the samples. They concluded that the amount of Al incorporation in FH was independent of the synthesis methods used but rather affected by the accumulated strain triggered by Al substitution in the FH lattice.

Ekstrom et al. (2010) explored the role of Al substitution on regulating the rate and extent of reduction of FH, GT, and lepidocrocite using the model dissimilatory Fe(III)-reducing bacterium (DIRB), *Shewanella putrefaciens*. The objective of the study was to predict the reducing strength of sediments on Fe (III)-based remediation techniques. FH samples were prepared using the synthesis method specified by Schwertmann and Cornell, 2000. A subset of the FH samples was also treated with pure quartz sand and sterilized by gamma irradiation to explore the impact of Al on FH reduction rates under conditions more representative of the natural environments. The samples were then analyzed using ICP analysis (to determine the Fe and Al content of the minerals), and BET (surface area determination by degassing for 24 h at $25^{o}$ C). Parameters such as particle size and shape of the crystals were described using TEM. The identification of synthesized mineral phases was conducted using XRD and EXAFS. Batch reduction experiments showed FH to inhibit microbial Fe (III) reduction in the presence of Al. The reduction rates of FH were also assessed to fall below those of lepidocrocite and GT at Al saturation levels equal to or greater than 18 mol% Al.

Masue et al. (2011) examined the impact of Al incorporation into the FH structure on its reductive dissolution and biotransformation by integrating both batch and advective flow column studies with Fe (II) and a bacterium (Shewanella sp. ANA-3). Also, they investigated the impact of ALSFH on the mobility of arsenic. Their results showed that structural Al diminishes the extent of FH reductive transformation. The reaction between the bacterium and the ALSFH showed that ALSFH dissolves incongruently at a faster rate compared to pure FH following the cessation of Fe (II)-induced transformation to secondary products. They also discovered the accelerated release of arsenic due to the reduced As (III) having a low affinity for the non-ferric sites formed from the reductive dissolution of ALSFH which results in the enrichment of Al sites.

The three studies described above all show the association of Al with FH to have significant effects on FH composition, structure, and surface properties such as area, particle size, abiotic dissolution rates, etc. Influence on the overall reactivity and interaction with organic and inorganic pollutants is also expected (Cismasu et al., 2012). However, the literature available till date reveals inconsistencies in the mode of Al association with FH. Cismasu et al. (2012) posited that variation in $Al^{3+}$ speciation in FH ranges from true isomorphous substitution for $Fe^{3+}$, to adsorption or surface precipitation, and to the formation of a mixture of two (or more) individual nanoscale phases. Varying concentrations of Al incorporation into FH structure have also been reported by different authors. For instance, Masue et al. (2007) reported 20 mol% Al, Schwertmann et al. (1979) reported 25 mol% Al, Harvey and Rhue (2008) reported approximately 82 mol% Al for synthetic 2LFH, and Chadwick et al. (1986) reported a maximum 92 mol% Al for 6LFH.

## 1.6 **Importance of ALSFH in the Removal of Oxyanions**

Selenate, phosphate, vanadate, chromate, and arsenate are some examples of oxyanions of key concern today (Adegoke et al., 2013). A well-known method for the removal of these oxyanions is "adsorption" onto various metal oxides and wastewater treatment residual due to advantages such as application at low concentrations, suitability for batch and continuous processes, and the overall reduction in sludge and waste material generation (Mohanty et al., 2006). As a result, several studies have explored the prevalence of ALSFH in the removal of harmful contaminants in the environments. Some pertinent examples are elucidated below.

Adra et al. (2013) studied the application of ALSFH in the treatment of arsenic contamination in a circumneutral pH river impacted by AMD. They examined contaminated sediments collected from the bed of the affected river and as well synthetic samples prepared by

neutralizing ferric nitrate solution with KOH. Al-bearing samples were prepared to yield various Al/Fe molar ratios. EXAFS spectroscopy conducted at the Fe K-edge showed that FH was the dominant mineral phase formed after the neutralization of the AMD. They also found Schwertmannite (an iron-oxyhydroxysulfate mineral) being transported in minute quantity from the AMD.

Harvey & Rhue (2008) combined both traditional batch techniques and flow adsorption micro-calorimetry to investigate the effects of Al/Fe saturation level on the kinetics and energetics of phosphate sorption and on the structural development in a multi-component $Al^{III}$ - $Fe^{III}$ sorbent system. They observed the Al content in the system to affect structural development and surface charge expressed as a function of Anion Exchange Capacity (AEC). The addition of more Al resulted in enhanced crystallization while the total energy of anion exchange was reported to exhibit a general increase with Al content. Higher structural development was also discovered to impact negatively phosphate sorption while higher AEC was accompanied by an increased phosphate sorption, as they expected.

Cismasu et al. (2011) characterized and compared FH samples collected from an AMD environment with 2LFH. Their results showed the level of impurity content in the FH samples to affect both the structural coherence and particle size while surface reactivity was inferred to be affected as a result of variability in surface composition, particle size, and aggregation properties. With increasing Al contents, a decline in particle size and an increase in structural disorder were observed.

Johnston & Chrysochoou (2016) using in-situ Attenuated Total Reflectance Fourier Transform Infrared spectroscopy (ATR-FTIR) studied the effect of the Al saturation level and pH on the adsorption mechanisms of chromate, selenate, and sulfate on FH. For the part of the study

involving sulfate, by using Multivariate Curve Resolution (MCR) to process obtained infrared spectra, they were able to characterize the structure and the influence of pH on the concentrations of synchronous sulfate species. Accordingly, they suggested that sulfate forms both outer-sphere and inner-sphere complexes on ALSFH with the bidentate setting primarily favored for the inner-sphere complexation. The main effect of Al incorporation into the FH structure however reported for this study was the suppression of the availability of inner-sphere binding sites.

Zhu et al. (2014) investigated the structure of sulfate adsorption complexes on FH using S K-edge XANES spectroscopy to determine whether sulfate forms inner- or outer-sphere complexes on Fe oxides. Based on the pre-edge feature observed in XANES, they suggested that some sulfate ions form inner-sphere complexes on FH surfaces. The structure of these sulfate inner-sphere complexes was then determined by EXAFS and d-PDF (Differential Pair Distribution Function) analyses.

Fukushi et al. (2013) using an extended triple-layer model (ETLM) as the predictive model for sulfate adsorption, obtained pH adsorption edges in the presence of sulfate as a function of ionic strength and initial sulfate concentration from batch adsorption experiments. Sulfate adsorption on FH was observed to increase continuously with decreasing pH and ionic strength.

There is quite an overwhelming evidence that the main mechanism of sulfate adsorption on FH is the outer sphere with some inner sphere at low pH and high coverage (Chrysochoou, 2016).

Sulfate was selected as the oxyanion for this thesis work. Sulfate occurs majorly in natural waters from soils to oceans and its concentrations in acidic water is enhanced by pyrite weathering in AMD (Swedlund et al., 2009; Zhang & Peak, 2007). Examining the adsorption behavior of sulfate with pH is important, as sulfate influences the adsorption properties of harmful dissolved

species often found coexisting with FH and hence affects their mobility in streams and soils (Fukushi et al., 2013). Sulfate binds to mineral surfaces from modification of their surface charge and many studies have been conducted on the resultant ternary surface complexes formed by the adsorption of sulfate on Fh (Zhu et al., 2014; Bazilevskaya et al., 2011; Johnston & Chrysochoou, 2016). The inhibiting effects of sulfate on mineral surfaces from competition for reactive sites have also been investigated by several authors (Swedlund et al., 2009; Ali & Dzonbak, 1996; Wijnja and Schulthess, 2002). Hence, the adsorption experiments conducted on both pure and ALSFH samples are important. Due to its high reactivity and large specific surface area, FH helps in the removal of inorganic pollutants such as sulfate, arsenic, antimony, from soils and surface waters (Dixit & Hering, 2003; Adra et al., 2013). Employing ALSFH is also important to replicate the conditions often found in natural environments where FH normally contains large amounts of impurities such as Al, presumably the outcome of co-precipitation processes (Bazilevskaya et al., 2011).

### 1.7 Purpose of the Study

Understanding the importance of iron hydr(oxide) in the fate and transport of contaminants in natural systems, the objective of this thesis work was to investigate the impact of Al substitution in FH on both its chemical and physical properties. Sulfate adsorption across pHs was selected as a probe for charge and adsorption properties to examine changes in chemical reactivity. For the physical properties, samples' morphology, specific surface area, crystallinity, and phase transformation upon heating were evaluated/parameterized to allow conclusions on the role of Al.

# 2 METHODS

## 2.1 Preparation of synthetic pure & Al-bearing Co-precipitated FH Samples

All mineral syntheses were performed with acid-washed glasswares, and all stock solutions were prepared with double deionized water *(*18.2 MΩ) and ACS grade chemicals, used as received.

Al-free 2LFH sample (0_ALSFH) was prepared based on Schwertmann and Cornell (2000) method. Specifically, 20g of $Fe(NO_3)_3.9H_2O$ was added to 250 mL DI water and neutralized to a pH of 7.5 with the incremental addition of freshly-made 1 M KOH, with stirring rate kept at 350 rpm. The first 150 mL of KOH was added in 5 min. The next 10 mL and last 2-3 mL were added dropwise at a rate of 0.5 mL $min^{-1}$ and 0.1-0.3 mL $min^{-1}$ respectively. After synthesis, the FH suspension was back-titrated to pH 4.6 with the addition of 60 mL of 0.1 M $HNO_3$ and stirred vigorously for 30 min at 500 rpm. The back-titration helped keep the FH suspension kinetically trapped since according to Schwertmann and Cornell (2000), FH can be held as a stable suspension in low pH away from the PZC where the surface charge of particles is increased. After the back-titration, centrifugation and dialysis followed to remove most of the residual ions (electrolytes). The suspension was dialyzed at 25$^o$ C against DI water for up to 4 days using 1 nm pore size Spectra/Por ® 7 dialysis membranes (molecular weight cut off of 1000) to remove entrained salts and Fe and Al species less than 1 nm. The water was changed several times daily until the conductivity dropped lower than 20μS $cm^{-1}$. The suspension was then collected and stored in polyethylene bottle for subsequent use.

ALSFH samples were prepared following the same protocol as the 0_ALSFH but by adding various volumes of the starting solutions proportional to the desired final mol % Al. These were 6 % Al, 12 % Al, 18 % Al, and 24 % Al abbreviated as 6_ALSFH, 12_ALSFH, 18_ALSFH, and 24_ALSFH throughout the text. Starting solutions of 1 L of 0.2 M $Fe(NO_3)_3.9H_2O$ and 0.2 L of

0.2 M $Al(NO_3)_3.9H_2O$ were prepared by adding 80.778g in 1 L of DI water and 15.0052g in 0.2 L of DI water respectively.

The suspensions' density for each ALSFH was estimated gravimetrically by drying a known volume of each suspension in an oven at $60^0$ C overnight (Table 1). This was subsequently used to obtain accurate mass in all experiments as described below.

**Table 1: Densities of FH Suspensions**

| Composition of Ferrihydrite | Density (g/L) | Standard deviation |
|---|---|---|
| 0_ALSFH | 8.86 | ± 0.31 |
| 6_ALSFH | 7.93 | ± 0.11 |
| 12_ALSFH | 6.99 | ± 0.09 |
| 18_ALSFH | 6.13 | ± 0.12 |
| 24_ALSFH | 5.47 | ± 0.36 |

## 2.2 Chemical Characterization

### *2.2.1 Chemical Composition by Acid Digestion*

Acid Digestion was used to determine the Al and total metal (Al + Fe) content of the ALSFH suspensions. A known mass (between 0.05g and 0.10 g) of air-dried sample collected from each ALSFH suspension was dissolved in 6 mL concentrated HCl and 4 mL concentrated $HNO_3$ inside a Teflon beaker. The Teflon beaker was heated in a heating block equipped with a temperature regulator for an hour. The analyte solution was then filled up to 50 mL with deionized

water before conducting Inductively Coupled Plasma Atomic Emission Spectroscopy (ICP-AES) analysis.

### *2.2.2 Sulfate Adsorption Envelopes*

The goal here was to construct sulfate adsorption envelopes as a function of solution pH. These envelopes were obtained in 0.01 M NaCl background electrolyte at an initial sulfate solution concentration of 1 mM. 1 g/L suspension of each ALSFH was prepared by adding the appropriate volumes of the $Na_2SO_4$ and NaCl stock solutions. A known amount of 1.0 M HCl or NaOH was then added to obtain a final supernatant pH values in the range of 3 to 9. Three replicates of each pH condition were shaken on an end-to-end shaker for 24 h after which time, each suspension was centrifuged and decanted, and supernatant filtered using a 0.2 $\mu$m syringe filter. The equilibrium pH of the supernatants was measured and final sulfate concentrations in the filtrate were measured using High-Performance Liquid Chromatography (HPLC) fitted with an ion conductivity detector (HPLC_IC).

It is noteworthy to say that the obtained equilibrium pHs (Appendix B.1-B.5) differed slightly from the adjusted pHs (3-9), as no measures were taken to exclude atmospheric $CO_2$ during the experiment. Accordingly, the equilibrium pHs have been used in the adsorption envelopes plots. However, for convenience, the initial pHs have been used in further discussion.

## 2.3 Heat Treatment Experiments

To further understand the role of Al substitution on FH, its transformation to more crystalline iron oxides (Hematite and Goethite) upon heating was investigated. Following findings by Burleson and Penn (2006) where FH aqueous suspensions aged at pH 10 and $90^0$ C were found to have completely converted from FH nanodots to goethite nanorods, 10 ml samples of each ALSFH suspensions held at slightly alkaline pHs were stored in tightly capped glass vials and aged

at $90^0$ C inside the oven for 48 hours. Samples were drawn from the initial vial at 0 h and subsequently at 12 h, 24 h, 36 h, and 48 h and stored under refrigeration until XRD and Electron Microscopy analyses were conducted as described below.

## 2.4 Physical Properties

### *2.4.1 Specific Surface Area Determination through BET Analysis*

BET analysis was performed to evaluate the specific surface area (SSA) ($m^2/g$) of each of the synthesized ALSFH samples. Multilayer nitrogen adsorption ($V_m$) expressed as a function of relative pressure ($P/P_o$) was measured using a fully automated surface area analyzer (Quantachrome's NOVA) equipped with the classical helium volumetric vacuum system.

Specific surface areas on air-dried samples were obtained from multipoint (BET) $N_2$ adsorption isotherms and analyzed using the Quantachrome NovaWin software. Samples were out-gassed prior to measurements for 19.0 h at $200.0^0$ C to remove any adsorbed volatile compounds from the surface.

### *2.4.2 Powder X-ray Diffraction (XRD)*

The structure of the ALSFH samples was examined by X-ray Diffraction. Each sample was prepared by pipetting tiny drops of the suspensions across a piece of tape ran across a sample holder, and air dried. Powder XRD patterns were then recorded with XPERT-PRO diffractometer: PANalytical measurement program (Figure 1), with a fixed $1^0$ divergence slit type and graphite monochromator (to reduce the fluorescence of Fe in samples) using CuK$\alpha$ radiation at generator settings (40 mA, 45 kV). Samples were scanned from $10.0231^0$ to $64.9611^0$ $2\theta$ in continuous scan mode, with step increments and counting time per step kept at $0.0260^0$ $2\theta$, and 121.8900 s respectively. The characteristic reflection peak (d-value) was matched with International Center

for Diffraction Data (ICDD) database, and its respective crystalline phase identified when appropriate.


**Figure 1. PANalytical XPERT-PRO XRD (Nikonova, 2015)**

### *2.4.3 Electron Microscopy Analysis*

#### *2.4.3.1 TEM combined with EDXS*

High-resolution transmission electron microscopy (HRTEM) characterization was carried out using a JEM 2100F (Figure 2) operating at an accelerating voltage of 200 kV (JEOL, Ltd. Tokyo Japan) at NanoEarth facility at Virginia Tech, Blacksburg VA. Samples were prepared by diluting 50μL of each ALSFH suspension in 500μL of methanol to prevent probable agglomeration. 1-3 drops of the diluted suspension were dropped on a copper specimen grid coated with an ultrathin layer of carbon (Ted Pella, Inc.). The grid was then placed under the hood to

allow the methanol to evaporate. Information on the sample elemental composition was collected using energy dispersive X-ray spectroscopy (EDXS; Oxford detector). Additionally, electron diffraction patterns were captured from selected areas on the samples for crystallinity and mineral verification. Micrographs taken at a 120-200kX and 400kX magnification were selected for further analyses using Gatan Digital Micrograph 2.1.1. These were analyzed to qualitatively describe samples morphological differences and to quantitatively parameterize the aspect ratio (Length/Width) of the observed particles in an attempt to parameterize any morphological differences and relate them to the Al substitution. Hematite (HM) and goethite (GT) particles were also tallied up across a set number of particles for each sample to obtain a qualitative HM/GT ratio.

**Figure 2. JEM-2100F Transmission Electron Microscope (Source: JEOL)**

# 3 RESULTS AND DISCUSSION

## 3.1 Chemical Composition by Acid Digestion

Compositional analyses (Table 2) of the ALSFH samples by ICP-AES revealed the desired mol % Al were not achieved in with the exception of the 0_ALSFH (pure FH) sample which returned a value approximately equal to the initial molar ratio of the Al- and Fe-nitrate solutions. The data indicated that 7.69% is the highest mol% achieved on the ALSFH. While the reason for this discrepancy is unknown to us at this moment, it seems that for the 6_ALSFH, 12_ALSFH, 18_ALSFH, and 24_ALSFH samples, a significant amount of their Al content might have leached out during dialysis. Another possibility for the substantial loss in the amount of Al present in the samples is the relatively high solubility of Al when certainly compared to $Fe^{III}$ solubility, considering the conditions of the FH synthesis (Cornell and Schwertmann, 2003). As these values will continue to be probed on another set of samples in the future samples, for convenience, the initial mol % Al values have been used in further discussion.

**Table 2: Composition of air-dried samples of the ALSFH suspensions**

| Sample | Fe (mg) | Al (mg) | Metal content (mmol/g) | Al (mol %) | Fe (mol %) | % Loss in Al |
|---|---|---|---|---|---|---|
| 0_ALSFH | 65.50 | 0.04 | 11.71 | 0.13 | 99.87 | No loss |
| 6_ALSFH | 31.66 | 0.69 | 11.82 | 4.34 | 95.66 | 27.67 |
| 12_ALSFH | 29.59 | 0.83 | 11.18 | 5.47 | 94.53 | 54.42 |
| 18_ALSFH | 54.80 | 2.06 | 10.55 | 7.23 | 92.77 | 59.83 |
| 24_ALSFH | 27.90 | 1.12 | 10.79 | 7.69 | 92.31 | 67.96 |

* Metal content (mmol/g; dry weight of FH samples digested)

However, a good indication of successful coprecipitation and perhaps substitution of Al with the FH is the plot (Figure 3) of the FH suspensions densities (g/L) against the % mol Al which returned a R-squared value of 0.9957 showing that as the lighter Al replaced the heavier Fe, the suspensions' densities did decrease in a manner proportional to the initial concentrations.

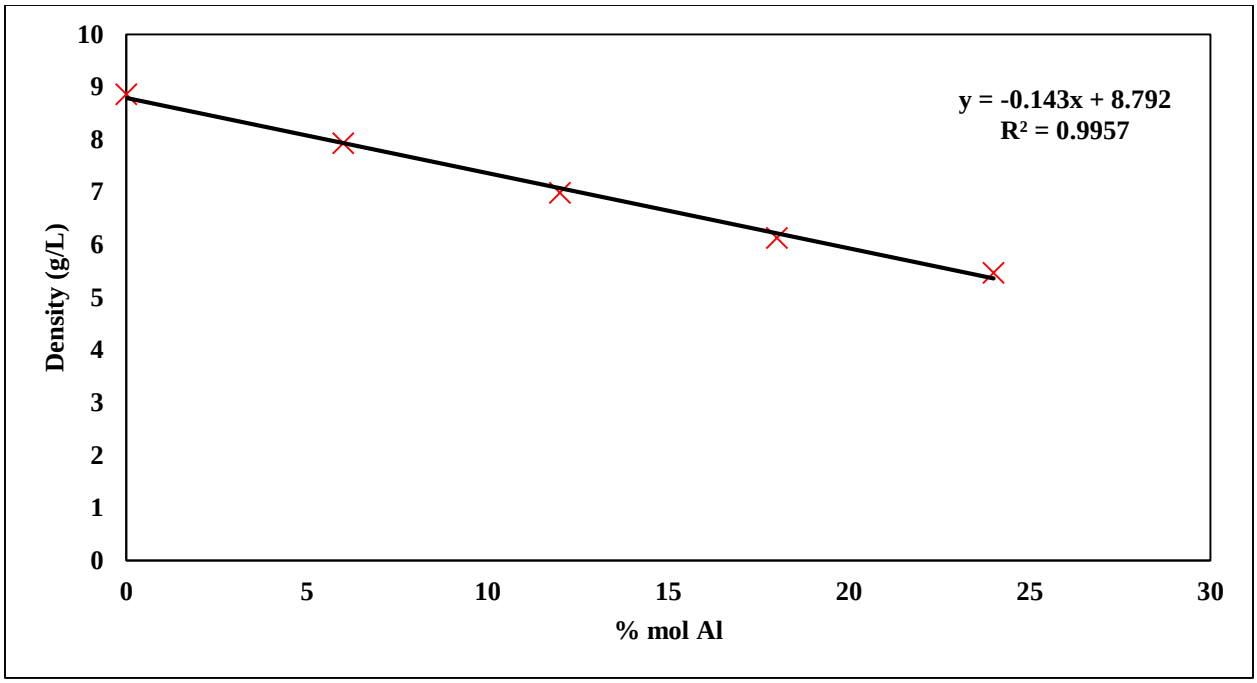


**Figure 3: Density (g/L) of FH suspensions vs % mol Al**

### 3.2 Sulfate Adsorption-Envelopes Experiments

Results from the conducted adsorption envelopes experiments (Figure 4) revealed a decrease in sulfate sorption for all the ALSFH samples as pH increased. This trend is also replicated when the amount of sulfate sorbed is normalized by the SSA of the FH samples (Figure 5). The 6_ALSFH sample (Figure 4B) exhibited a significant drop in sulfate sorption from pH 3-7 and experienced a slight increase as it crossed the neutral pH relative to the 0_ALSFH sample. The ALSFH samples with 12% Al, 18% Al, and 24% Al composition (Figure 4C, 4D, and 4E respectively) showed an upward trend in sulfate sorption, and this trend was more pronounced in the strongly acidic domain (pH 3-5). Also, in the acidic region, the 24_ALSFH sample had the most sulfate sorption of all the FH samples with over 90% sorption observed at strongly acidic pH 3-4.

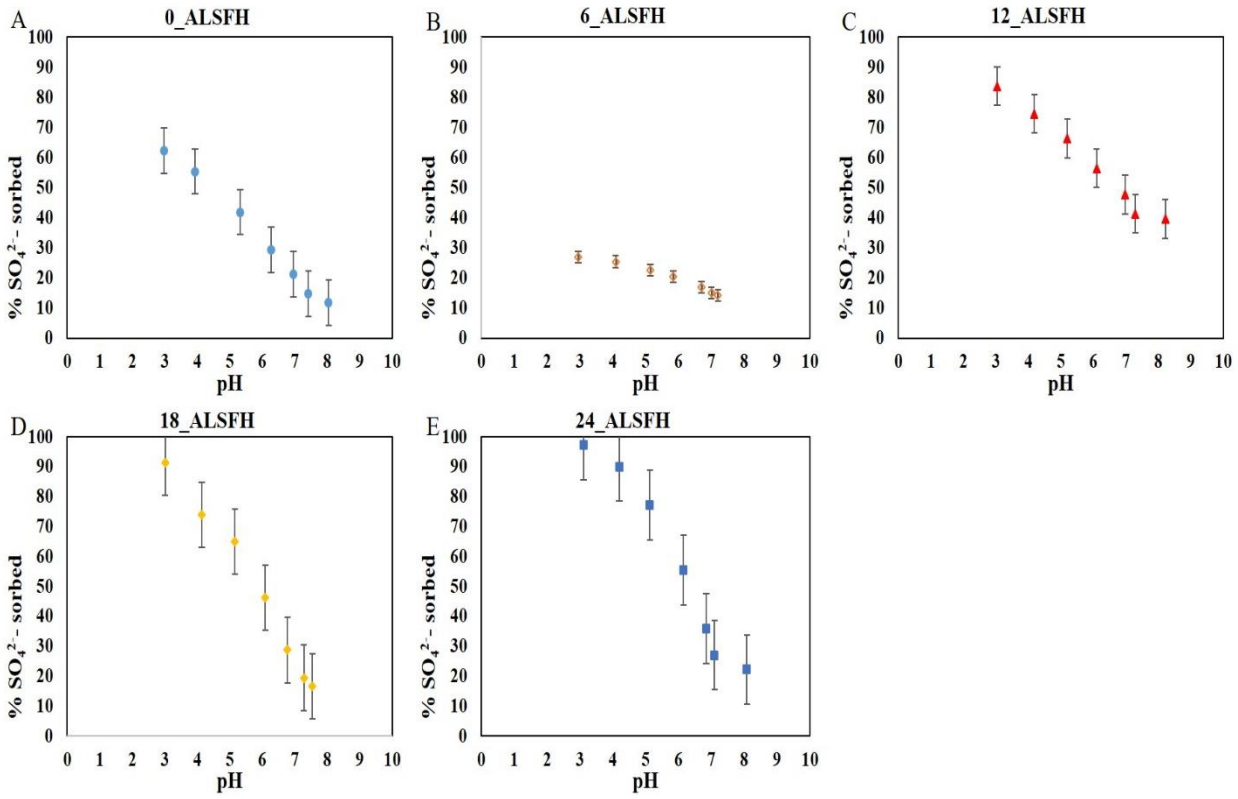


**Figure 4. Sulfate pH-adsorption envelopes for pure and Al-substituted FH. Error bars have been plotted by specifying the values of standard errors obtained for each adsorption envelope experiment as both positive and negative error values**

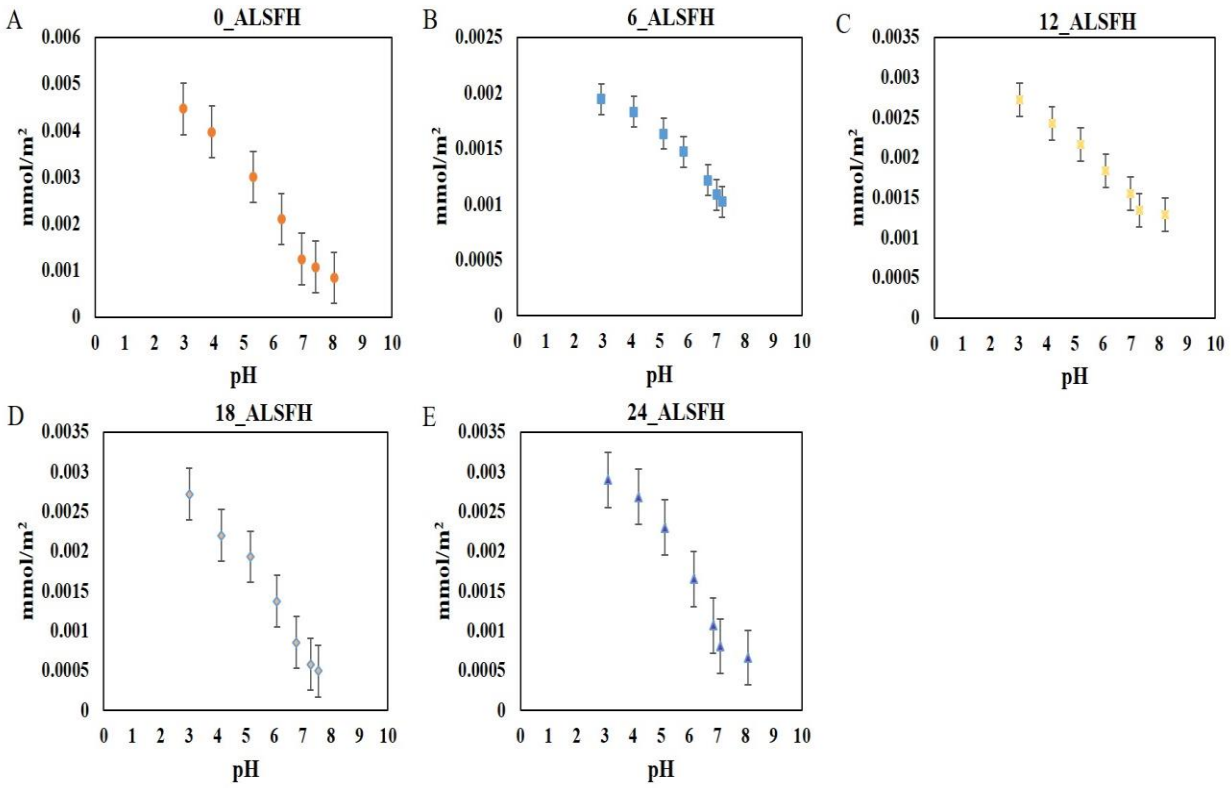


**Figure 5. Sulfate pH-adsorption envelopes for pure and Al-substituted FH normalized with measured SSA**

Figure 4 portrays the adsorption envelopes of sulfate on FH in 10mM NaCl solution as background electrolyte and 1mM $Na_2SO_4$ as reacting solution. For any of the ALSFH samples, the amount of sulfate adsorption increased with the decrease in pH. This trend is characteristic of oxyanion sorption on metal oxides (Harvey & Rhue, 2008) and has been corroborated by many studies. For instance, in a study conducted by Fukushi et al. (2013), using an extended triple-layer model (ETLM) as the predictive model for sulfate adsorption, pH adsorption edges in the presence of sulfate as a function of ionic strength and sulfate concentration were obtained from batch adsorption experiments. The sulfate adsorption on FH was observed to increase continuously with decreasing pH and ionic strength. Harvey and Rhue (2008) studied the kinetics and energetics of phosphate sorption in a multi-component Al(III)-Fe(III) hydr(oxide) sorbent system using a

combination of traditional batch techniques and flow adsorption calorimetry. Their investigation showed that phosphate sorption on the hydr(oxides) followed a typical two-step trend where sorption rates are initially high but decreases as the availability of sorption sites on the oxide surface decreases.

A closely similar "relative" reduction in sorption (Figure 6) was observed across pH 4-9 using the percentage function of the difference between sorption at these pHs and pH 3. The region of greatest loss in sorption coincided with pH 9 pointing at a strong inhibiting effect at this pH across all the ALSFH samples.

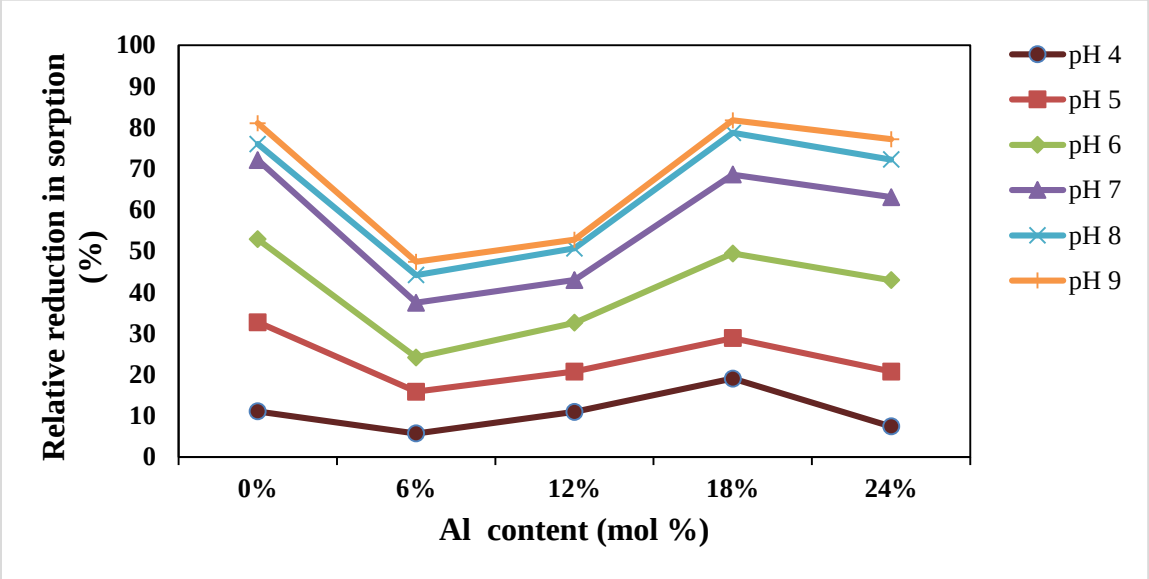


**Figure 6. Relative reduction in sorption over pH range 4-9 across all ALSFH samples**

Gimenez et al. (2007) studied the sorption of As (III) and As (V) on different natural oxides (hematite, magnetite, and goethite). They observed that variation in the arsenic sorbed in response to pH corresponded with a decrease in sorption on the three sorbents at alkaline pH values. This observation was replicated in the trend observed for sorption loss represented in (Figure 6) where the region corresponding to the greatest relative reduction in sulfate sorption was observed at pH 9. Naeem et al. (2007) in assessing vanadium removal by three commercially available metal oxide

adsorbents used the influence of pH, vanadium concentration, and volume/mass ratio as a probe. Vanadium adsorption was observed here to decrease with increasing pH, with maximum adsorption capacities achieved at pH 3-4.

According to Parks (1965), and Schwertmann and Taylor (1977), synthetic Fe oxides are well documented to have their PZC within the range pH 7–9. PZC is an important parameter often used in characterizing the protonation (positive surface sites) and deprotonation (negative surface sites) behavior of hydr(oxides) in aqueous suspensions (Bourikas et al., 2005). The affinity of mineral surfaces to ionic surfactants or polyelectrolytes which help modify their surface properties is defined by the position of their PZC (Adegoke et al., 2013). As a consequence, FH shows a positive charge at pHs less than the PZC and anions are likely to be adsorbed. In the pH-adsorption envelope experiments conducted, the initially high sulfate sorption (pH 3-4) recorded for the FH samples (Figure 4) regardless of their Al content can be attributed to the presence of positive reactive sites on the mineral surface below the PZC thereby aiding ion or ligand exchange. An upward shift in PZC due to increasing Al content as observed by Cismasu et al. (2013) could explain the high sorption rates seen in the 24_ALSFH sample.

The incorporation of a structural impurity such as Al in FH has been shown by many authors to influence the stability of the hydrous ferric oxide by limiting its structural development into more crystalline phases (Cornell & Schwertmann, 2003; Bazilevskaya et al., 2011; Johnston & Chrysochoou, 2016). Several studies have also investigated the effects of Al on surface properties of hydr(oxides) and the mobility of organic and inorganic contaminants in aqueous environments (Masue et al., 2007; Jain et al., 2009; Manceau & Gates, 2013). Observing the plotted sorption data (Figure 4), it can be seen that the ALSFH sample with 6 % Al saturation level (Figure 4B) experienced approximately 56 % reduction in sorption amount when compared to the

pure FH sample (Figure 4A) at pH 3. This reduction was also observed for the 6_AlSFH within pH 4-7. The amount of sulfate sorbed however increased with Al content for the other ALSFH samples (12_ALSFH, 18_ALSFH, and 24_ALSFH) (Figure 4C, 4D, and 4E respectively). Therefore, understanding the behavior observed for the different ALSFH samples (particularly the negative effect on sorption in the 6_ASFH sample) requires characterizing the effects of Al substitution on the adsorption mechanisms of sulfate (Johnston & Chrysochoou, 2016).

Referencing findings by Zhu et al. (2014) and Johnston & Chrysochoou (2016) on the surface structure and reactivity of ALSFH, the significant loss in sorption observed in the 6_ALSFH sample (Figure 4B) may be the result of limited well-ordered reactive sites triggered by the effects of Al on the growth of the Fe hydr(oxide) nuclei. The surge recorded in the level of sorption for the 12_ALSFH, 18_ALSFH, and 24_ALSFH samples (Figure 4C, 4D, and 4E respectively) may also be the result of the significant increase in the relative fraction of outer-sphere complexes for sulfate with increasing Al substitution. By observing Johnston & Chrysochoou (2016)'s finding on the inhibition of the occurrence of sulfate sorption via inner-sphere ligand exchange due to increasing Al content, the mechanism of sulfate sorption on the FH samples may be assumed to be the outcome of simple ion exchange occurring via outer-sphere complexation. The possibility that the outer sphere complexation may involve a crystalline Al phase (e.g. gibbsite or boehmite with PZC typically around 9-10) where sulfate is being increasingly exchanged with more Al substitution shouldn't be ruled out. However, this hypothesis can only be tested by finding whether Al is inside the FH structure or precipitated out as a separate phase.

Implicatively, experiments aimed at understanding the mechanisms through which oxyanions (particularly sulfate) are adsorbed by ALSFH will be my future focus.

### 3.3 SSA through BET Analysis

From the Multi-Point BET plots (Appendix D.1-D.5), the SSAs of the 0_ALSFH, 6_ALSFH, 12_ALSFH, 18_ALSFH, 24_ALSFH samples were 136.41 $m^2/g$, 139.26 $m^2/g$, 312.17 $m^2/g$, 343.16 $m^2/g$, 336.25 $m^2/g$ respectively. However, it is important to note that these obtained BET SSA values are indicative of the exposed surface area of dry sample aggregates. These values considerably underestimate the actual SSA to be derived from the samples when suspended in aqueous solutions. This is due to the larger particle aggregation that ensues upon drying such synthesized nanoparticles (Villalobos and Antelo, 2011).

A "non-linear" upward trend was observed in SSA with more Al substitution into the structure of FH. The difference in the SSAs can be attributed to the impact of Al substitution on the physical properties of the FH samples such as particle size and morphology. As will be discussed later on using the evidence gathered from XRD analysis, with more Al, less transformation to more crystalline phases was seen thereby ensuring that the ALSFH samples persisted as FH for an extended period of time. Also, the BET SSA values of 136.41 $m^2/g$ and 336.25 $m^2/g$, for 0_ALSFH and 24_ALSFH, respectively, strongly suggest a definitive size difference between both FH samples. Hence, using the obtained SSAs as proxies for the particle size of each FH sample, the crystallite size in nm (Figure 7) can be obtained using the linear relationship [SSABET = -72.741(Crystallite Size in nm) + 558.91] derived by Villacís-García et al., 2015 by recalculating the data by Wang et al. (2013). Accordingly, the particle size for 0_ALSFH, 6_ALSFH, 12_ALSFH, 18_ALSFH, and 24_ALSFH was respectively 5.83 nm, 5.80 nm, 3.41 nm, 2.98 nm, and 3.07 nm. A decline in particle size was accompanied by a corresponding increase in SSA. The particle sizes derived also agreed with the particle size range (2 to 9nm) specified by Hiemstra (2013) for FH to be considered a nanomineral.

To obtain the SSA of individual FH particles (actual SSA), the actual SSA was related to the inverse relationship between particle diameter *d* (nm) and SSA [SSA = (6/ρ)/*d*, where ρ = 3.57 g/cm$^3$ is the mass density for 2LFH; Murphy et al., 1976]. Hence, the calculated actual SSA of 0_ALSFH, 6_ALSFH, 12_ALSFH, 18_ALSFH, and 24_ALSFH was respectively 288.04 $m^2g^{-1}$, 290.00 $m^2g^{-1}$, 493.22 $m^2g^{-1}$, 564.05 $m^2g^{-1}$, and 546.57 $m^2g^{-1}$. These values assume the individual FH particles to possess a spherical shape (Villalobos and Antelo, 2011) and agree with the SSA of >200 $m^2g^{-1}$ reported by Weidler (1997) and Dzombak & Morel (1990).

The determined SSAs of the FH samples are vital in predicting how the bioavailability of pure and ALSFH in environmental settings influences their application as sorbent systems for contaminants cleaning.

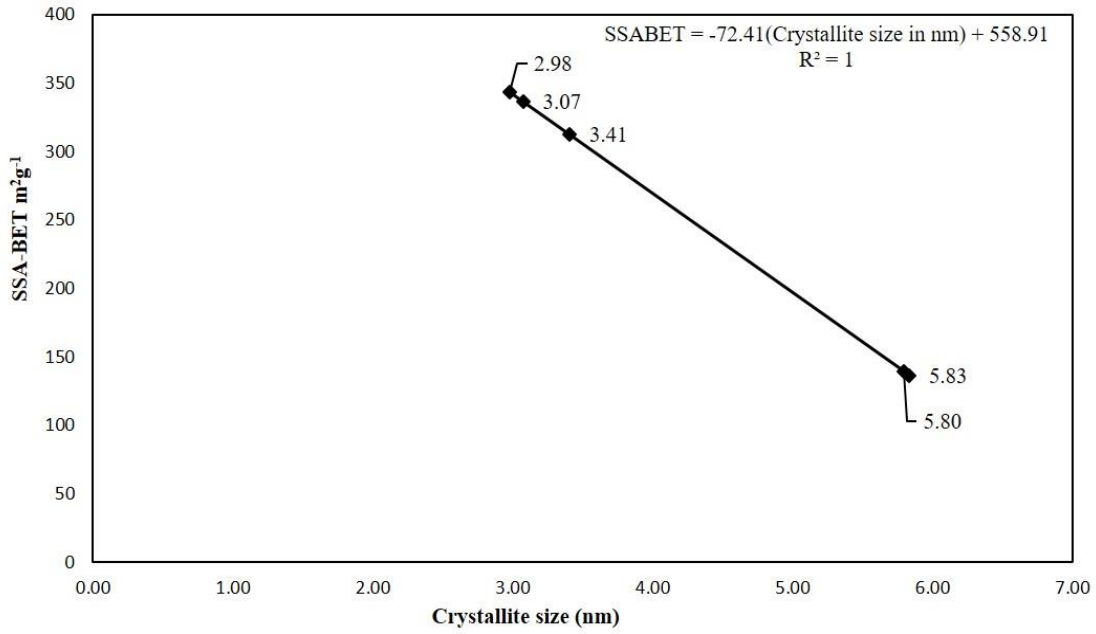


**Figure 7. Linear relationship between particle size (nm) and BET-SSA**

## 3.4 XRD Analysis

### *3.4.1 X-ray diffractograms for unaged (0 h) nanoparticles*

The characteristic reflection peaks (*d*-values) from the XRD analysis of samples were matched to the ICDD database (Card no. 29-0713) for phase identification. Peaks (110) indicative of goethite (GT: α-FeOOH) were identified in the XRD spectra (Figure 8). No other Fe oxide phases particularly the two bands characteristic of 2LFH usually centered at $2\theta$ of $35^0$ and $63^0$ according to Schwertmann and Cornell (2007) were identified. The samples had been kept in the lab at room temperature for more than five months before analysis. It seems that the stability of the suspensions may have been compromised and some FH to GT transformations have already occurred. Also, no peaks confirming the presence of separate aluminum phases (gibbsite, boehmite) were observed in the diffraction data. This may be due to the possibility that the Al phases could have been amorphous. A detection problem could have also stemmed from the relatively small amount of analyte pipetted on the tape attached to the sample holder. It is highly doubted that the volume of the ALSFH suspension dropped on the tape contained as much as ~ 2 % by mol Al for XRD to pick a boehmite or a gibbsite signal.

From the appearance of the XRD spectra, differences in the relative crystallinities of the samples were deduced by observing changes in the peak widths and heights. The 0_ALSFH exhibited a tall and sharp peak denoting high crystallinity. However, the peak became broader and lower as more Al was added (6_ALSFH, 12_ALSFH, and 18_ALSFH) indicating a decreasing crystallinity until it completely disappeared at 24_ALSFH. This trend corroborated the findings by several studies (Cornell and Schwertmann, 2003; Bazilevskaya et al., 2011; Johnston & Chrysochoou, 2016) positing that Al incorporation into FH impedes crystal growth.

Also, the results from the XRD analysis matched those obtained from measuring the SSAs of the samples. Summarily, crystallinity (0_ALSFH > 6_ALSFH > 12_ALSFH >18_ALSFH > 24_ALSFH) decreased with increasing SSA (136.41 $m^2/g$ < 139.26 $m^2/g$ < 312.17 $m^2/g$ < 343.16 $m^2/g$ < 336.25 $m^2/g$).

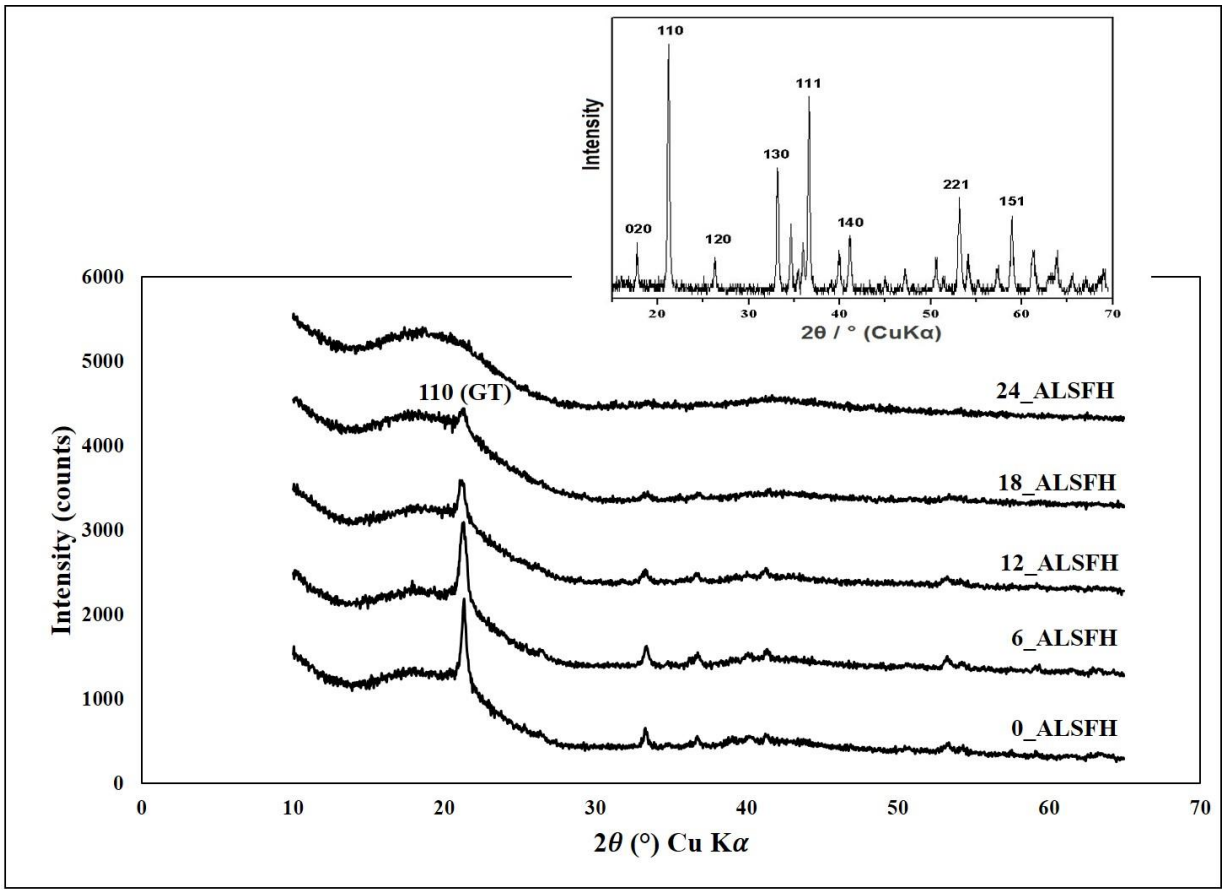


**Figure 8. X-ray diffraction patterns for unaged nanoparticles. The inset picture shows the hkl indices of Goethite (ICDD Card no. 29-0713)**

### *3.4.2 X-ray diffractograms for aged (12 h, 24 h, 36 h, and 48 h) nanoparticles*

The results obtained from the time-lapse aging experiments (Figure 9) modelled those previously gathered from the unaged samples except for the appearance or persistence of the goethite peak in the 24_AlSFH samples. The goethite peak for the 24_ALSFH sample, as well as

for all other substitutions, increased with time (12 h < 24 h < 36 h < 48 h) highlighting the increased transformation of FH into GT upon heating. It is noteworthy to mention that the previously noted Al impact still held upon heating, whereby an increased Al content resulted in a lower overall transformation into GT as witnessed by the inverse relation between the size of the GT peak and the Al content in the ALSFH samples This trend and the lack of an XRD peak indicating the other crystalline and thermodynamically stable end product (for e.g. HM) within the ferrihydrite aggregate prompted an investigation by Electron Microscopy aimed at understanding the influence of temperature on the rate of conversion of FH to crystalline oxides. Findings from this investigation are discussed in the paragraphs below.

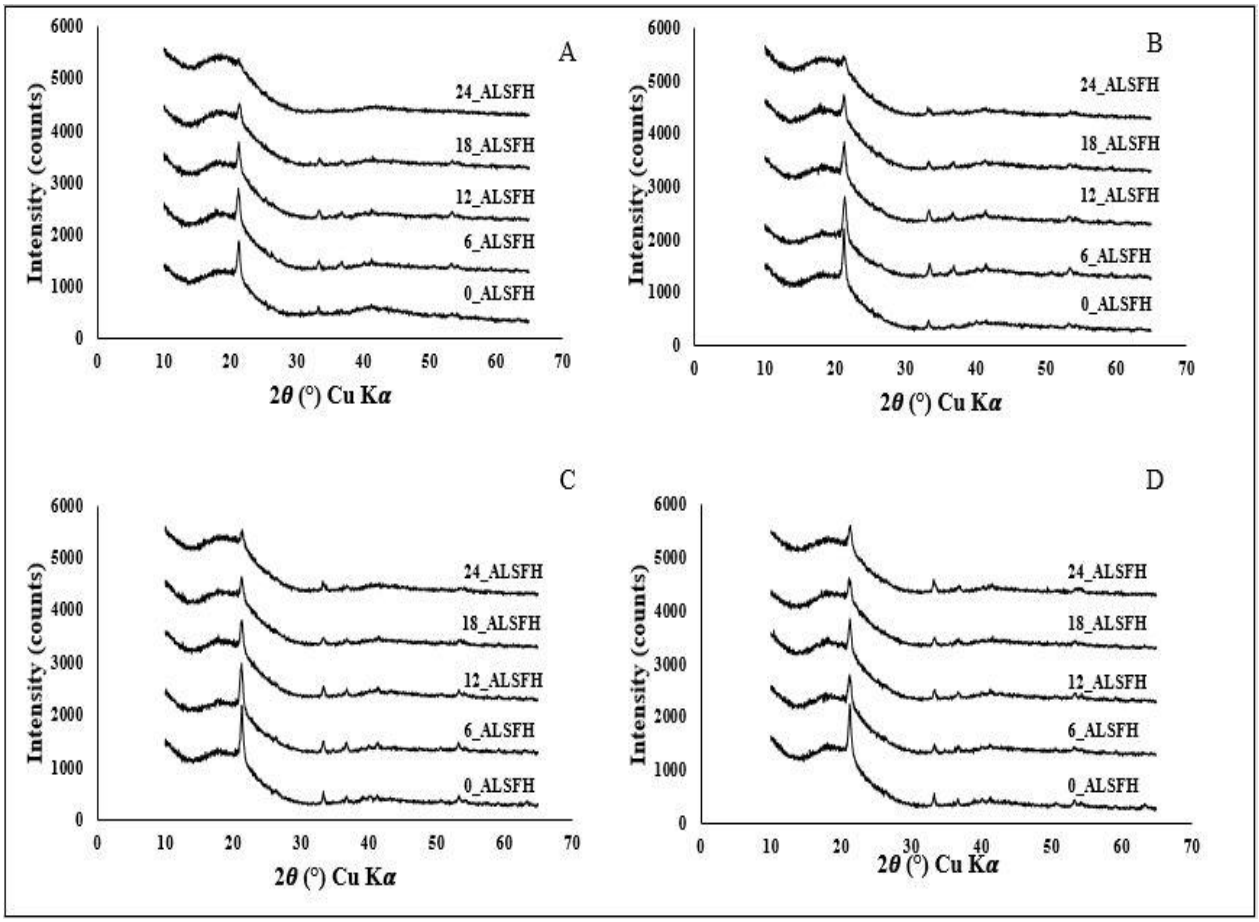


**Figure 9. XRD patterns for nanoparticles aged at (A) 12 h, (B) 24 h, (C) 36 h, and (D) 48 h**

### 3.5 TEM analysis combined with EDXS

TEM characterization of the unaged nanoparticles (Figure 10) revealed that FH nanodots in the 0_ALSFH were aggregated and significantly transformed to acicular crystals of goethite nanorods. This is again the result of the transformation occurring at room temperature, despite the suspensions being stored at low pH, away from their ZPC. However, the incorporation of Al into the FH structure retarded the transformation and fewer goethite nanorods were observed for the 6_ALSFH, 12_ALSFH, and 18_ALSFH respectively. Both 0_ALSFH and 6_ALSFH samples also showed evidence of hematite (HM: $\alpha$-$Fe_2O_3$) crystals with grainy appearance. Further incorporation of Al into the FH structure favored the appearance of lenticular crystals of HM in the 12_ALSFH sample. The HM crystals in the 18_ALSFH sample were the largest and exhibited transitional forms with hexagonal outline but lobed edges (Schwertmann et al., 1979). These results again showcased the transformation of the FH suspensions at room temperature in the time-scale of 5 months. A strong inhibiting effect of Al substitution in the FH structure was seen in the 24_ALSFH sample which contains predominantly small aggregated spheres of FH nanoparticles. This is confirmed by the lack of crystalline peak in the XRD pattern (Figure 8) for the 24_ALSFH sample.

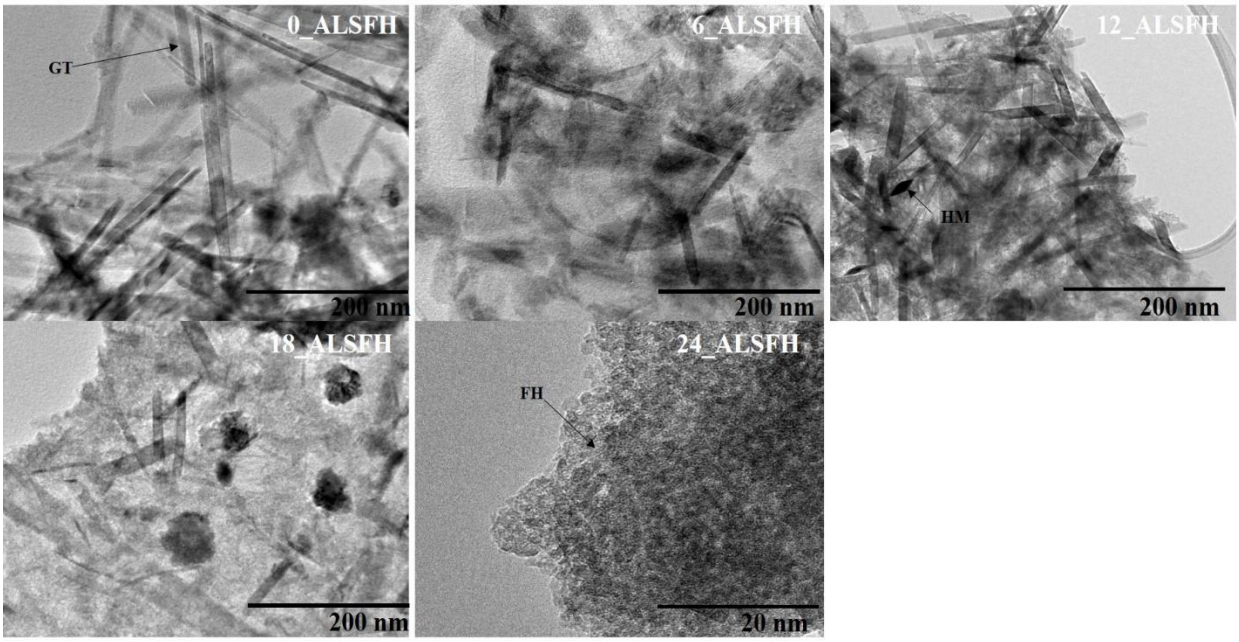


**Figure 10. Representative TEM micrographs of unaged ALSFH samples**

Table 3 presents the result of the semi-quantitative parameterization of the aspect ratio of the mineral particles observed under HRTEM. The mineral particle dimensions (Table 3) calculated showed a decrease in aspect ratio of the goethite nanorods with increasing Al substitution. This trend has been previously observed for Al-substituted goethite (Burleson and Penn, 2006; Ekstrom et al., 2010; Schulze and Schwertmann, 1987). Ekstrom et al. (2010) findings showed goethite particles without Al to exhibit multidomainic acicular crystals while more Al replacements favored monodomainic crystals with decreasing aspect ratio.

**Table 3: Particle dimensions (L/W) of GT crystals found in unaged samples**

| Sample* | Aspect Ratio (L/W) | Standard deviation |
|---|---|---|
| 0_ALSFH | 32.7 | ± 3.7 |
| 6_ALSFH | 8.4 | ± 1.9 |
| 12_ALSFH | 8.3 | ± 2.1 |
| 18_ALSFH | 7.5 | ± 1.4 |

* Data on particle dimensions for the 24_ALSFH sample is unavailable as no crystalline phase was observed

The impact of heating on crystal growth for all the ALSFH samples is well reflected in the electron micrographs of the samples heated at 48 h (Figure 11). In the 0_ALSFH sample, a complete phase transformation of the FH nanoparticles to GT and HM was observed. Also, blocky laths of GT crystals were found interspersed with acicular GT crystals while the HM crystals were well-developed when compared to the grainy appearance observed for HM in the unaged 0_ALSFH sample (Figure 10). Heat also modified particle morphology for both the GT and HM crystals in all the ALSFH samples. With more Al substitution, an increase was observed in the amount and sizes of the HM crystals. It can be observed qualitatively that more HM particles are in the 24_ALSFH sample. Hence, it was concluded that the inhibiting effect of Al in this case was less effective when compared to the unaged 24_ALSFH (Figure 10) where no phase transformation of the FH nanoparticles occurred.

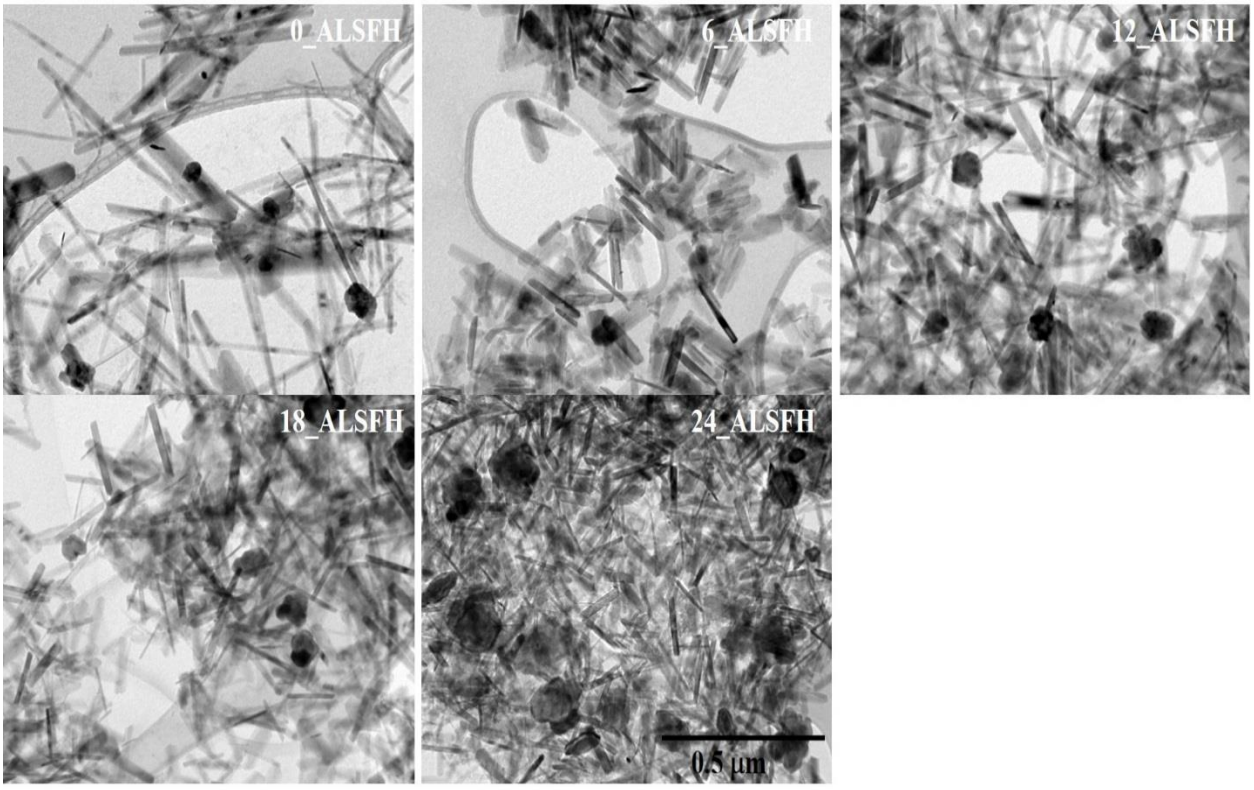


**Figure 11. Representative TEM micrographs of FH samples aged at 90° C for 48 h**

Under the influence of heat, a decrease in aspect ratio of the GT crystals in the 6_ALSFH (Table 4) was immediately observed after the introduction of Al into the FH structure. However, no significant difference was seen across the 12_ALSFH and 18_ALSFH samples before an eventual decline in aspect ratio for the 24_ALSFH sample.

Results from these TEM micrographs modelled the XRD patterns (Figure 9) collected for all the ALSFH samples after heat treatment for 48 hours. However, XRD failed to pick any peak for the HM crystals. This could be due to the low overall concentration of HT in the samples which is below the detection limit of the XRD. Lastly, it is important to note that although the ALSFH heated suspensions were sampled at 12 h, 24h, and 36 h also, micrographs collection from these time points is still underway and will be included as soon as finished. These will be valuable in obtaining an understanding of the speed of the FH transformation and whether it is similar for both GT and HT.

**Table 4: Particle dimensions (L/W) of GT crystals found in samples aged for 48 h**

| Sample | Aspect Ratio (L/W) | Standard deviation |
|---|---|---|
| 0_ALSFH | 19.5 | ± 7.3 |
| 6_ALSFH | 7.1 | ± 1.8 |
| 12_ALSFH | 9.5 | ± 2.8 |
| 18_ALSFH | 9.9 | ± 3.9 |
| 24_ALSFH | 6.9 | ± 1.6 |

The EDX spectrum (Figure 12A) of the spot analyzed in the 0_ALSFH sample did not have any peak for Al indicating the original conditions set during synthesis. The corresponding EDX spectra (Figure 12B, 12C, 12D, and 12E) collected from spots in the 6_ALSFH, 12_ALSFH, 18_ALSFH, and 24_ALSFH samples respectively, all indicated Al peaks which continued to grow with more substitution of Al into the FH structure.

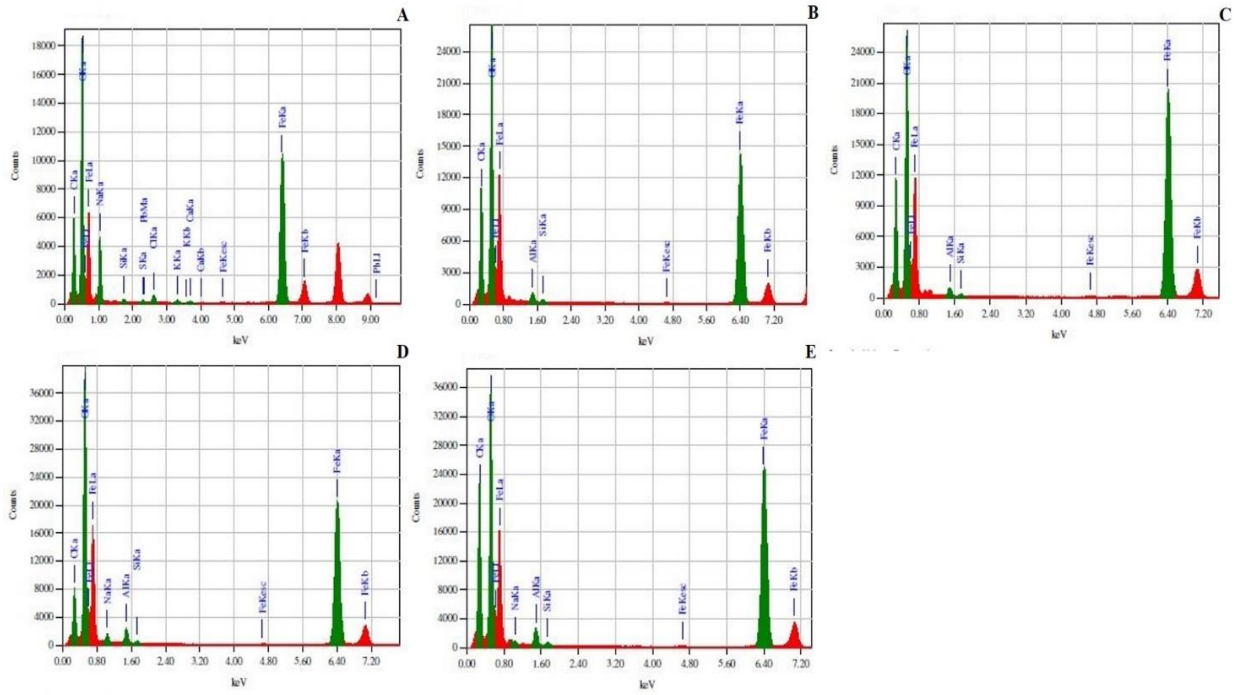


**Figure 12. EDX spectrographs of FH samples aged at 90° C for 48 h**

* Refer to Appendix F1-F5 for clearer spectrographs

# 4 CONCLUSIONS

The conducted adsorption envelopes experiments revealed an increase in pH to cause a decline in the amount of sulfate adsorbed on all the ALSFH samples. Sulfate adsorption was most pronounced at acidic pHs with more Al substitution into the FH structure favoring an upward trend in this oxyanion's adsorption within the acidic domain after an initial decline with the introduction of Al in the 6_ALSFH sample. A closely similar "relative reduction" in sorption was also observed across all pHs with pH 9 corresponding to the region where adsorption was most inhibited.

Using SSA through BET analysis as a probe for a physical property such as particle size for the FH samples, an increase in SSA was accompanied by a corresponding decrease in particle size. This indicated Al substitution affects crystallite size. This is because of the inhibiting effect Al has on FH growth and crystallization.

XRD analysis was also used to evaluate phase transformation of the FH samples (aged and unaged). Peaks (110) indicative of goethite (GT) were identified in the XRD spectra. No other Fe oxide phases or Al oxide peaks confirming the presence of separate aluminum phases were observed in the diffraction data for both sample series. However, the incorporation of Al influenced peak widths and heights and impeded crystal growth.

TEM micrographs were collected and helped with the identification of morphological differences in all the samples. For both sample series, FH nanodots were found to have transformed to GT and HM crystals. GT crystals were either acicular or as blocky laths depending on the amount of Al in the FH structure while the HM crystals had either grainy appearance, were lenticular, or were platy crystals with lobed edges. Noteworthy in the unaged samples was the retardation of crystal growth by Al substitution which was most prominent in the unaged

24_ALSFH sample where aggregated spheres of FH nanoparticles persisted. This effect was however removed under the influence of heat as evident in the aged 24_ALSFH sample.

Conclusively, Al as a structural impurity affects the physicochemical properties of FH nanoparticles such as SSA, particle size, surface reactivity, and stability of the mineral.

# 5 FUTURE CONSIDERATIONS

In the future, the impact of Al substitution on the acid dissolution behavior of the FH samples will be explored. This will provide an insight on understanding whether the co-precipitation of Al with the FH samples occurs congruently (i.e. indication that both Al and Fe dissolve at equal rates) or incongruently. Also, according to Cornell and Schwertmann (2003), the dispersal of Al throughout the entire mineral phase rather than concentration on the surface or discrete domains within the hydr(oxide) can be used as a proxy for isomorphic substitution which is a function of congruent dissolution. To that effect elemental map using electron microscopy will be further helpful in identifying the location of the Al in these samples.

Understanding the mechanism of formation of both GT and HM crystals in FH in the presence of Al-containing solution will also be the subject of future study. The idea that GT forms from ALSFH through a solution phase and that HM nucleates and forms within FH aggregates will be tested to see if the Al content in both crystals is increased by the Al-containing solution or solely Al coprecipitated during the synthesis of FH. TEM micrographs for the 12 h, 24 h, and 36 h time-points will be collected and used alongside existing micrographs (Unaged and 48 h) to further test this hypothesis.

The effect of Al content on sorption energetics of FH nanoparticles will also be explored in the future by collecting data on the heat of sulfate sorption and flow adsorption calorimetry will be used to elucidate the effects of sulfate sorption on the surface properties of the ALFH sorbent system.

## REFERENCES

Adegoke, H. I., Adekola, F. A., Fatoki, O. S., & Ximba, B. J. (2013). Sorptive interaction of oxyanions with iron oxides: a review. *Pol. J. Environ. Stud*, *22*(1), 7.

Adra, A., Morin, G., Ona-Nguema, G., Menguy, N., Maillot, F., Casiot, C., … Brest, J. (2013). Arsenic Scavenging by Aluminum-Substituted Ferrihydrites in a Circumneutral pH River Impacted by Acid Mine Drainage. *Environmental Science & Technology*, *47*(22), 12784–12792. http://doi.org/10.1021/es4020234

Alarcón, R., Gaviria, J., & Dold, B. (2014). Liberation of Adsorbed and Co-Precipitated Arsenic from Jarosite, Schwertmannite, Ferrihydrite, and Goethite in Seawater. *Minerals*, *4*(3), 603–620. http://doi.org/10.3390/min4030603

Ali, M.A., Dzombak, D.A., 1996. Competitive sorption of simple organic acids and sulfate on goethite. *Environ. Sci. Technol*. 30, 1061–1071.
DOI: 10.1021/es940723g

Antelo, J., Fiol, S., Pérez, C., Mariño, S., Arce, F., Gondar, D., & López, R. (2010). Analysis of phosphate adsorption onto ferrihydrite using the CD-MUSIC model. *Journal of Colloid and Interface Science*, *347*(1), 112–119. http://doi.org/10.1016/j.jcis.2010.03.020

Bazilevskaya, E., Archibald, D. D., Aryanpour, M., Kubicki, J. D., & Martínez, C. E. (2011). Aluminum coprecipitates with Fe (hydr)oxides: Does isomorphous substitution of Al3+ for Fe3+ in goethite occur? *Geochimica et Cosmochimica Acta*, *75*(16), 4667–4683. http://doi.org/10.1016/j.gca.2011.05.041

Beal, E. J., House, C. H., & Orphan, V. J. (2009). Manganese- and Iron-Dependent Marine Methane Oxidation. *Science*, *325*(5937), 184. https://doi.org/10.1126/science.1169984

Bourikas K., Kordulis C., Lycoughiotis A. (2005). Differential Potentiometric Titration: Development of a Methodology for determining the point of zero charge of metal (hydr)oxides by one Titration curve. *Environ. Sci. Technol*. 39, 4100.

Burleson, D. J., & Penn, R. L. (2006). Two-Step Growth of Goethite from Ferrihydrite. *Langmuir*, *22*(1), 402–409. https://doi.org/10.1021/la051883g

Carlson, L., & Schwertmann, U. (1981). Natural ferrihydrites in surface deposits from Finland and their association with silica. *Geochimica et Cosmochimica Acta*, *45*(3), 421–429. https://doi.org/10.1016/0016-7037(81)90250-7

Cheng, S., Jang, J.-H., Dempsey, B. A., & Logan, B. E. (2011). Efficient recovery of nano-sized iron oxide particles from synthetic acid-mine drainage (AMD) water using fuel cell technologies. *Water Research*, *45*(1), 303–307. https://doi.org/10.1016/j.watres.2010.07.054

Childs, C. W. (1992), Ferrihydrite: A review of structure, properties and occurrence in relation to soils. Z. Pflanzenernaehr. Bodenk., 155: 441–448. doi:10.1002/jpln.19921550515

Cismasu, A. C., Levard, C., Michel, F. M., & Brown, G. E. (2013). Properties of impurity-bearing ferrihydrite II: Insights into the surface structure and composition of pure, Al- and Si-bearing ferrihydrite from Zn(II) sorption experiments and Zn K-edge X-ray absorption spectroscopy. *Geochimica et Cosmochimica Acta*, *119*, 46–60. https://doi.org/10.1016/j.gca.2013.05.040

Cismasu, A. C., Michel, F. M., Stebbins, J. F., Levard, C., & Brown Jr., G. E. (2012). Properties of impurity-bearing ferrihydrite I. Effects of Al content and precipitation rate on the structure of 2-line ferrihydrite. *Geochimica et Cosmochimica Acta, 92*, 275–291. http://doi.org/10.1016/j.gca.2012.06.010

Cismasu, A. C., Michel, F. M., Tcaciuc, A. P., Tyliszczak, T., & Brown, J., Gordon E. (2011). Composition and structural aspects of naturally occurring ferrihydrite. *Comptes Rendus Geoscience*, *343*(2–3), 210–218. http://doi.org/10.1016/j.crte.2010.11.001

Cornell, R. M., & Schwertmann, U. (1979). Influence of organic anions on the crystallization of ferrihydrite. *Clays Clay Miner*, *27*(6), 402–410.

Cornell, R. M., & Schwertmann, U. (2003) The Iron Oxides-Structure, Properties, Reactions, Occurrences and Uses. Darmstadt: Wiley–VCH GmbH & Co. KGaA.

Dixit, S., and Hering, J. (2003). Comparison of Arsenic(V) and Arsenic(III) Sorption onto Iron Oxide Minerals: Implications for Arsenic Mobility. *Environmental Science & Technology 37* (18), 4182-4189 DOI: 10.1021/es030309t

Drits, V. A., Sakharov, B. A., Salyn, A. L., & Manceau, A. (1993). Structural model for ferrihydrite. *Clay Minerals*, *28*, 185–185.

Dzombak D.A. and Morel F.M.M. (1990). Surface complexation modeling. Hydrous ferric oxide. John Wiley. New York, 393 pp.

Ekstrom, E. B., Learman, D. R., Madden, A. S., & Hansel, C. M. (2010). Contrasting effects of Al substitution on microbial reduction of Fe(III) (hydr)oxides. *Geochimica et Cosmochimica Acta*, *74*(24), 7086–7099. http://doi.org/10.1016/j.gca.2010.09.008

Fleischer, M., Chao, G. Y., and Kato, A. (1975) New mineral names: Am. Mineral. 60, 485-486.

Fu, D., Keech, P. G., Sun, X., & Wren, J. C. (2011). Iron oxyhydroxide nanoparticles formed by forced hydrolysis: dependence of phase composition on solution concentration. *Phys. Chem. Chem. Phys.*, *13*(41), 18523–18529. http://doi.org/10.1039/C1CP20188C

Fukushi, K., Aoyama, K., Yang, C., Kitadai, N., & Nakashima, S. (2013). Surface complexation modeling for sulfate adsorption on ferrihydrite consistent with in situ infrared spectroscopic

observations. *Applied Geochemistry*, *36*, 92–103. http://doi.org/10.1016/j.apgeochem.2013.06.013

Gilbert, B., Lu, G., & Kim, C. S. (2007). Stable cluster formation in aqueous suspensions of iron oxyhydroxide nanoparticles. *Journal of Colloid and Interface Science*, *313*(1), 152–159. http://doi.org/10.1016/j.jcis.2007.04.038

Gimenez, J., Martinez, M., Depablo, J., Rovira, M., & Duro, L. (2007). Arsenic sorption onto natural hematite, magnetite, and goethite. *Journal of Hazardous Materials*, *141*(3), 575–580. http://doi.org/10.1016/j.jhazmat.2006.07.020

Harvey, O. R., & Rhue, R. D. (2008). Kinetics and energetics of phosphate sorption in a multi-component Al(III)–Fe(III) hydr(oxide) sorbent system. *Journal of Colloid and Interface Science*, *322*(2), 384–393. http://doi.org/10.1016/j.jcis.2008.03.019

Hiemstra, T. (2013). Surface and mineral structure of ferrihydrite. *Geochimica et Cosmochimica Acta*, *105*, 316–325. https://doi.org/10.1016/j.gca.2012.12.002

Hiemstra, T., & Van Riemsdijk, W. H. (2009). A surface structural model for ferrihydrite I: Sites related to primary charge, molar mass, and mass density. *Geochimica et Cosmochimica Acta*, *73*(15), 4423–4436. https://doi.org/10.1016/j.gca.2009.04.032

Hofmann, A., Beinum, W. van, Meeussen, J. C. L., & Kretzschmar, R. (2005). Sorption kinetics of strontium in porous hydrous ferric oxide aggregates II. Comparison of experimental results and model predictions. *Journal of Colloid and Interface Science*, *283*(1), 29–40. http://doi.org/http://dx.doi.org/10.1016/j.jcis.2004.08.105

Hrischeva, E., & Scott, S. D. (2007). Geochemistry and morphology of metalliferous sediments and oxyhydroxides from the Endeavour segment, Juan de Fuca Ridge. *Geochimica et Cosmochimica Acta*, *71*(14), 3476–3497. https://doi.org/10.1016/j.gca.2007.03.024

Jain, A., Sharma, V. K., & Mbuya, O. S. (2009). Removal of arsenite by Fe(VI), Fe(VI)/Fe(III), and Fe(VI)/Al(III) salts: effect of pH and anions. *Journal of Hazardous Materials*, *169*(1–3), 339–344. http://doi.org/10.1016/j.jhazmat.2009.03.101

Jambor, J. L., & Dutrizac, J. E. (1998). Occurrence and Constitution of Natural and Synthetic Ferrihydrite, a Widespread Iron Oxyhydroxide. *Chemical Reviews*, *98*(7), 2549–2586. https://doi.org/10.1021/cr970105t

Johnston, C., & Chrysochoou, M. (2016). Mechanisms of Chromate, Selenate, and Sulfate Adsorption on Al-Substituted Ferrihydrite: Implications for Ferrihydrite Surface Structure and Reactivity. *Environmental Science & Technology* 2016 *50* (7), 3589-3596 DOI: 10.1021/acs.est.5b05529

Kabengi, N. J., Daroub, S. H., & Rhue, R. D. (2006). Energetics of arsenate sorption on amorphous aluminum hydroxides studied using flow adsorption calorimetry. *Journal of Colloid and Interface Science*, *297*(1), 86–94. http://doi.org/10.1016/j.jcis.2005.10.050

Liu, H., Li, X., Wang, Y., Yang, X., Zhen, Z., Chen, R., … Wei, Y. (2014). New insight into the effect of the formation environment of ferrihydrite on its structure and properties. *RSC Adv.*, *4*(22), 11451–11458. http://doi.org/10.1039/C4RA00696H

Maillot, F., Morin, G., Wang, Y., Bonnin, D., Ildefonse, P., Chaneac, C., & Calas, G. (2011). New insight into the structure of nanocrystalline ferrihydrite: EXAFS evidence for tetrahedrally coordinated iron(III). *Geochimica et Cosmochimica Acta*, *75*(10), 2708–2720. https://doi.org/10.1016/j.gca.2011.03.011

Manceau, A. and Gates, W. (2013). Incorporation of Al in iron oxyhydroxides: implications for the structure of ferrihydrite. *Clay Miner. 48* (3), 481-489.

Masue-Slowey, Y., Loeppert, R. H., & Fendorf, S. (2011). Alteration of ferrihydrite reductive dissolution and transformation by adsorbed As and structural Al: Implications for As retention. *Geochimica et Cosmochimica Acta*, *75*(3), 870–886. http://doi.org/10.1016/j.gca.2010.11.016

Masue, Y., Loeppert, R., & Kramer, T. A. (2007). Arsenate and Arsenite Adsorption and Desorption Behavior on Coprecipitated Aluminum:Iron Hydroxides. *Environmental Science & Technology*, *41*(3), 837–842. http://doi.org/10.1021/es061160z

Michel, F. M., Ehm, L., Antao, S. M., Lee, P. L., Chupas, P. J., Liu, G., … Parise, J. B. (2007). The Structure of Ferrihydrite, a Nanocrystalline Material. *Science*, *316*(5832), 1726. https://doi.org/10.1126/science.1142525

Mohanty, K., Das, D., & Biswas, M. N. (2006). Preparation and characterization of activated carbons from Sterculia alata nutshell by chemical activation with zinc chloride to remove phenol from wastewater. *Adsorption*, *12*(2), 119–132. https://doi.org/10.1007/s10450-006-0374-2

Murphy P.J., Posner A.M. and Quirk J.P. (1976). Characterization of partially neutralized ferric nitrate solutions. J. Colloid Interface Sci. 56, 270-283.

Naeem, A., Westerhoff, P., & Mustafa, S. (2007). Vanadium removal by metal (hydr)oxide adsorbents. *Water Research*, *41*(7), 1596–1602. http://doi.org/10.1016/j.watres.2007.01.002

Nagata, T., Fukushi, K., & Takahashi, Y. (2009). Prediction of iodide adsorption on oxides by surface complexation modeling with spectroscopic confirmation. *Journal of Colloid and Interface Science*, *332*(2), 309–316. http://doi.org/10.1016/j.jcis.2008.12.037

Navrotsky, A., Mazeina, L., & Majzlan, J. (2008). Size-Driven Structural and Thermodynamic Complexity in Iron Oxides. *Science*, *319*(5870), 1635. https://doi.org/10.1126/science.1148614

Nikonova, Elena L., "Authigenic Clay Formation and Diagenetic Reactions, Lake Magadi, Kenya." Thesis, Georgia State University, 2016. http://scholarworks.gsu.edu/geosciences_theses/88

Parfitt, R. L., Van der Gaast, S. J., & Childs, C. W. (1992). A structural model for natural siliceous ferrihydrite. *Clays and Clay Minerals*, *40*, 675–675.

Pariona, N., Camacho-Aguilar, K. I., Ramos-González, R., Martinez, A. I., Herrera-Trejo, M., & Baggio-Saitovitch, E. (2016). Magnetic and structural properties of ferrihydrite/hematite nanocomposites. *Journal of Magnetism and Magnetic Materials*, *406*, 221–227. https://doi.org/10.1016/j.jmmm.2016.01.001

Pham, A. L.-T., Doyle, F. M., & Sedlak, D. L. (2012). Kinetics and efficiency of H2O2 activation by iron-containing minerals and aquifer materials. *Water Research*, *46*(19), 6454–6462. https://doi.org/10.1016/j.watres.2012.09.020

Russell, J. D. (1979) Infrared spectroscopy of ferrihydrite: Evidence for the presence of structural hydroxyl groups: Clay Miner. 14, 109-113.

Schulze D. G. and Schwertmann U. (1987) The influence of aluminum on iron oxides. XIII: Properties of goethites synthesized in 0.3 M KOH at 25 C. Clay Miner. 22, 83–92.

Schwertmann, U., & Cornell, R. M. (2008). *Iron Oxides in the Laboratory*. Wiley. Retrieved from https://books.google.com/books?id=yfOrDwOvCYkC

Schwertmann, Udo & Cornell, R. M & Wiley InterScience (Online service) (2000). Iron oxides in the laboratory : preparation and characterization (2nd completely rev. and extended ed). Wiley-VCH, Weinheim ; New York

Spadini, L., Schindler, P. W., Charlet, L., Manceau, A., & Vala Ragnarsdottir, K. (2003). Hydrous ferric oxide: evaluation of Cd–HFO surface complexation models combining CdK EXAFS data, potentiometric titration results, and surface site structures identified from mineralogical knowledge. *Journal of Colloid and Interface Science*, *266*(1), 1–18. http://doi.org/10.1016/S0021-9797(03)00504-6

Sposito, G., 1989. *The Chemistry of Soils (Chaps. 8 and 9)*. New York: Oxford University Press, 277 pp.

Sullivan, L. A., & Bush, R. T. (2004). Iron precipitate accumulations associated with waterways in drained coastal acid sulfate landscapes of eastern Australia. *Marine and Freshwater Research*, *55*(7), 727–736.

Swedlund, P. J., Webster, J. G., & Miskelly, G. M. (2009). Goethite adsorption of Cu(II), Pb(II), Cd(II), and Zn(II) in the presence of sulfate: Properties of the ternary complex. *Geochimica et Cosmochimica Acta*, *73*(6), 1548–1562. http://doi.org/10.1016/j.gca.2008.12.007

Towe, K. M. and Bradley, W. F. (1967) Mineralogical constitution of colloidal "hydrous Ferric oxides": J. Colloid Interface Sci. 24, 383-392.

Villacis-García, M., Ugalde-Arzate, M., Vaca-Escobar, K., Villalobos, M., Zanella, R., & Martinez villegas, N. (2015). Synthesis in laboratory of goethite and ferrihydrite of sizes of particle controlled. Bulletin of the society geological Mexican, 67 (3), 433-446.

Villalobos, M., & Antelo, J. (2011). A unified surface structural model for ferrihydrite: Proton charge, electrolyte binding, and arsenate adsorption. *Rev. Int. Contam. Ambie*, *27*, 139–151.

Wang, X., Li, W., Harrington, R., Liu, F., Parise, J.B., Feng, X., Sparks, D.L. 2013, Effect of ferrihydrite crystallite size on phosphate adsorption reactivity: Environmental Science and Technology, 47, 10322-10331.

Weatherill, J. S., Morris, K., Bots, P., Stawski, T. M., Janssen, A., Abrahamsen, L., … Shaw, S. (2016). Ferrihydrite Formation: The Role of $Fe_{13}$ Keggin Clusters. *Environmental Science & Technology*, *50*(17), 9333–9342. http://doi.org/10.1021/acs.est.6b02481

Weidler, P. G. (1997). BET Sample Pretreatment of Synthetic Ferrihydrite and its Influence on the Determination of Surface Area and Porosity. *Journal of Porous Materials*, *4*(3), 165–169. https://doi.org/10.1023/A:1009610800182

Wijnja, H., & Schulthess, C. P. (2002). Effect of Carbonate on the Adsorption of Selenate and Sulfate on Goethite Storrs Agric. Exp. Stn. Scientific Contribution no. 1917. *Soil Science Society of America Journal*, *66*(4), 1190–1197. http://doi.org/10.2136/sssaj2002.1190

Zhang, G. Y., & Peak, D. (2007). Studies of Cd(II)–sulfate interactions at the goethite–water interface by ATR-FTIR spectroscopy. *Geochimica et Cosmochimica Acta*, *71*(9), 2158–2169. http://doi.org/10.1016/j.gca.2006.12.020

Zhu, M., Northrup, P., Shi, C., Billinge, S. J. L., Sparks, D. L., & Waychunas, G. A. (2014). Structure of Sulfate Adsorption Complexes on Ferrihydrite. *Environmental Science & Technology Letters*, *1*(1), 97–101. http://doi.org/10.1021/ez400052r

# APPENDICES

## Appendix A: Densities of FH suspensions

| Composition of Ferrihydrite | Density (g/L) | Standard deviation (S.D) |
|---|---|---|
| 0_ALSFH | 8.86 | ± 0.31 |
| 6_ALSFH | 7.93 | ± 0.11 |
| 12_ALSFH | 6.99 | ± 0.09 |
| 18_ALSFH | 6.13 | ± 0.12 |
| 24_ALSFH | 5.47 | ± 0.36 |
| | | |
| Specification of parameters used for the adsorption envelopes experiments | | |
| ApHX | | |
| BpHX | | |
| CpHX | | |
| DpHX | | |
| EpHX | | |
| Where | | |
| X = 1, 2, 3 (sample number) | | |
| A = 0_ALSFH | | |
| B = 6_ALSFH | | |
| C = 12_ALSFH | | |
| D = 18_ALSFH | | |
| E = 24_ALSFH | | |

## Appendix B: pH's of supernatants used for HPLC analysis

### *Appendix B.1: pH Determination for 0_ALS*FH

| Samples | pH of Supernatant | | | | |
|---|---|---|---|---|---|
| | 1 | 2 | 3 | Mean pH | S. D |
| A3 [3.00] | 2.97 | 2.98 | 2.98 | 2.98 | ± 0.01 |
| A4 [4.01] | 3.92 | 3.94 | 3.93 | 3.93 | ± 0.01 |
| A5 [5.02] | 5.44 | 5.29 | 5.24 | 5.32 | ± 0.10 |
| A6 [6.02] | 6.2 | 6.32 | 6.3 | 6.27 | ± 0.06 |
| A7 [6.99] | 7.02 | 6.97 | 6.89 | 6.96 | ± 0.07 |
| A8 [8.03] | 7.4 | 7.4 | 7.46 | 7.42 | ± 0.03 |
| A9 [9.04] | 8.11 | 8.11 | 7.92 | 8.05 | ± 0.11 |

Initial pH of 1L solution = 8.28
[adjusted pH]
Na2SO4 (1mM) = 0.142042 g  Weighed Na2SO4 (1mM) = 0.1431 g
NaCl (10mM) = 0.58443 g  Weighed NaCl (10mM) = 0.5847 g
Volume equivalent of 1g of A = 112.87g

### *Appendix B.2: pH Determination for 6_ALS*FH

| Samples | pH of Supernatant | | | | |
|---|---|---|---|---|---|
| | 1 | 2 | 3 | Mean pH | S. D |
| B3 [3.01] | 2.94 | 2.94 | 2.96 | 2.95 | ± 0.01 |
| B4 [4.03] | 4.09 | 4.09 | 4.1 | 4.09 | ± 0.01 |
| B5 [5.03] | 5.18 | 5.12 | 5.14 | 5.15 | ± 0.03 |
| B6 [6.00] | 5.83 | 5.84 | 5.85 | 5.84 | ± 0.01 |
| B7 [7.00] | 6.67 | 6.71 | 6.74 | 6.71 | ± 0.04 |
| B8 [8.03] | 7.06 | 7.01 | 6.94 | 7.00 | ± 0.06 |
| B9 [9.04] | 7.18 | 7.18 | 7.24 | 7.20 | ± 0.03 |

Initial pH of 1L solution = 8.15
[adjusted pH]
Required Na2SO4 (1mM) = 0.142042 g  Weighed Na2SO4 (1mM) = 0.1423 g
Required NaCl (10mM) = 0.58443 g  Weighed NaCl (10mM) = 0.5838 g
Volume equivalent of 1g of B = 126.10 mL

***Appendix B.3: pH Determination for 12_ALS*FH**

| Samples | pH of Supernatant | | | | |
|---|---|---|---|---|---|
| | 1 | 2 | 3 | Mean pH | S. D |
| C3 [3.02] | 3.06 | 3.03 | 3.03 | 3.04 | ± 0.02 |
| C4 [3.99] | 4.2 | 4.21 | 4.15 | 4.19 | ± 0.03 |
| C5 [5.02] | 5.2 | 5.22 | 5.19 | 5.20 | ± 0.02 |
| C6 [6.01] | 6.05 | 6.12 | 6.14 | 6.10 | ± 0.05 |
| C7 [7.02] | 7.01 | 6.97 | 6.96 | 6.98 | ± 0.03 |
| C8 [8.04] | 7.28 | 7.26 | 7.35 | 7.30 | ± 0.05 |
| C9 [8.99] | 8.24 | 8.21 | 8.2 | 8.22 | ± 0.02 |

Initial pH of 1L solution = 8.33
[adjusted pH]
Required Na2SO4 (1mM) = 0.142042 g
Weighed Na2SO4 (1mM) = 0.1430 g
Required NaCl (10mM) = 0.58443 g
Weighed NaCl (10mM) = 0.5852 g
Volume equivalent of 1g of C = 143.06 mL

***Appendix B.4: pH Determination for 18_ALS*FH**

| Samples | pH of Supernatant | | | | |
|---|---|---|---|---|---|
| | 1 | 2 | 3 | Mean pH | S. D |
| D3 [3.02] | 3.01 | 3 | 3.02 | 3.01 | ± 0.01 |
| D4 [4.01] | 4.13 | 4.14 | 4.15 | 4.14 | ± 0.01 |
| D5 [5.01] | 5.22 | 5.15 | 5.12 | 5.16 | ± 0.05 |
| D6 [6.00] | 6.12 | 6.08 | 6.09 | 6.10 | ± 0.02 |
| D7 [6.98] | 6.78 | 6.85 | 6.71 | 6.78 | ± 0.07 |
| D8 [8.01] | 7.29 | 7.3 | 7.25 | 7.28 | ± 0.03 |
| D9 [9.01] | 7.6 | 7.54 | 7.49 | 7.54 | ± 0.06 |

Initial pH of 1L solution = 8.23
[adjusted pH]
Required Na2SO4 (1mM) = 0.142042 g
Weighed Na2SO4 (1mM) = 0.1426 g
Required NaCl (10mM) = 0.58443 g
Weighed NaCl (10mM) = 0.5845 g
Volume equivalent of 1g of D = 163.13 mL

***Appendix B.5: pH Determination for 24_ALS*FH**

| Samples | pH of Supernatant | | | | |
|---|---|---|---|---|---|
| | 1 | 2 | 3 | Mean pH | S. D |
| E3 [3.02] | 3.12 | 3.1 | 3.13 | 3.12 | ± 0.02 |
| E4 [4.03] | 4.19 | 4.2 | 4.21 | 4.20 | ± 0.01 |
| E5 [5.00] | 5.17 | 5.13 | 5.1 | 5.13 | ± 0.04 |
| E6 [6.05] | 6.13 | 6.16 | 6.18 | 6.16 | ± 0.03 |
| E7 [7.03] | 6.9 | 6.84 | 6.8 | 6.85 | ± 0.05 |
| E8 [8.06] | 7.16 | 7.1 | 7.04 | 7.10 | ± 0.06 |
| E9 [9.00] | 8.05 | 8.11 | 8.1 | 8.09 | ± 0.03 |

Initial pH of 1L solution = 8.44
[adjusted pH]
Required Na2SO4 (1mM) = 0.142042 g
Required NaCl (10mM) = 0.58443 g
Volume equivalent of 1g of E = 182.8 mL

Weighed $Na_2SO_4$ (1mM) = 0.1420 g
Weighed NaCl (10mM) = 0.5846 g

## Appendix C: HPLC Data

### *Appendix C.1: Adsorption data for 0_ALSFH*

| Samples | Dilution factor | Diluted conc. (mg/L) | Amount sorbed (mg/L) | Amount sorbed (mM) |
|---|---|---|---|---|
| A31 | 1 | 36.62 | 57.39 | 0.60 |
| A32 | 1 | 35.24 | 58.77 | 0.61 |
| A33 | 1 | 34.71 | 59.30 | 0.62 |
| A41 | 1 | 42.57 | 51.44 | 0.54 |
| A42 | 1 | 42.26 | 51.75 | 0.54 |
| A43 | 1 | 41.14 | 52.87 | 0.55 |
| A51 | 1 | 53.61 | 40.40 | 0.42 |
| A52 | 1 | 56.38 | 37.63 | 0.39 |
| A53 | 1 | 53.98 | 40.03 | 0.42 |
| A61 | 1 | 66.81 | 27.20 | 0.28 |
| A62 | 1 | 65.04 | 28.97 | 0.30 |
| A63 | 1 | 67.49 | 26.52 | 0.28 |
| A71 | 1 | 78.97 | 15.04 | 0.16 |
| A72 | 1 | 75.55 | 18.46 | 0.19 |
| A73 | 1 | 78.57 | 15.44 | 0.16 |
| A81 | 1 | 80.85 | 13.16 | 0.14 |
| A82 | 1 | 81.06 | 12.95 | 0.13 |
| A83 | 1 | 77.96 | 16.05 | 0.17 |
| A91 | 1 | 83.85 | 10.16 | 0.11 |
| A92 | 1 | 83.39 | 10.62 | 0.11 |
| A93 | 1 | 81.53 | 12.48 | 0.13 |

Initial $SO_4^{2-}$ conc. = 94.009 mg/L
Molar mass of $SO_4^{2-}$ = 96.06 g/mol

***Appendix C.2: Adsorption data for 6_ALSFH***

| Samples | Dilution factor | Diluted conc. (mg/L) | Amount sorbed (mg/L) | Amount sorbed (mM) |
|---|---|---|---|---|
| B31 | 1 | 70.68 | 25.84 | 0.27 |
| B32 | 1 | 70.35 | 26.17 | 0.27 |
| B33 | 1 | 70.54 | 25.98 | 0.27 |
| B41 | 1 | 72.63 | 23.89 | 0.25 |
| B42 | 1 | 71.39 | 25.12 | 0.26 |
| B43 | 1 | 72.01 | 24.51 | 0.26 |
| B51 | 1 | 75.02 | 21.50 | 0.22 |
| B52 | 1 | 74.41 | 22.11 | 0.23 |
| B53 | 1 | 74.50 | 22.02 | 0.23 |
| B61 | 1 | 77.11 | 19.41 | 0.20 |
| B62 | 1 | 76.89 | 19.63 | 0.20 |
| B63 | 1 | 76.43 | 20.09 | 0.21 |
| B71 | 1 | 80.82 | 15.70 | 0.16 |
| B72 | 1 | 79.48 | 17.04 | 0.18 |
| B73 | 1 | 80.46 | 16.06 | 0.17 |
| B81 | 1 | 82.22 | 14.30 | 0.15 |
| B82 | 1 | 82.24 | 14.28 | 0.15 |
| B83 | 1 | 81.54 | 14.98 | 0.16 |
| B91 | 1 | 81.96 | 14.56 | 0.15 |
| B92 | 1 | 83.12 | 13.40 | 0.14 |
| B93 | 1 | 83.46 | 13.06 | 0.14 |

Initial $SO_4^{2-}$ conc. = 96.518 mg/L
Molar mass of $SO_4^{2-}$ = 96.06 g/mol

***Appendix C.3: Adsorption data for 12_ALSFH***

| Samples | Dilution factor | Diluted conc. (mg/L) | Amount sorbed (mg/L) | Amount sorbed (mM) |
|---|---|---|---|---|
| C31 | 1 | 16.01 | 81.65 | 0.85 |
| C32 | 1 | 16.00 | 81.67 | 0.85 |
| C33 | 1 | 15.88 | 81.79 | 0.85 |
| C41 | 1 | 24.29 | 73.38 | 0.76 |
| C42 | 1 | 24.26 | 73.41 | 0.76 |
| C43 | 1 | 26.21 | 71.46 | 0.74 |
| C51 | 1 | 32.97 | 64.69 | 0.67 |
| C52 | 1 | 32.93 | 64.74 | 0.67 |
| C53 | 1 | 32.90 | 64.77 | 0.67 |
| C61 | 1 | 42.57 | 55.10 | 0.57 |
| C62 | 1 | 42.64 | 55.03 | 0.57 |
| C63 | 1 | 42.59 | 55.08 | 0.57 |
| C71 | 1 | 51.05 | 46.61 | 0.49 |
| C72 | 1 | 51.14 | 46.53 | 0.48 |
| sC73 | 1 | 50.99 | 46.68 | 0.49 |
| C81 | 1 | 57.43 | 40.24 | 0.42 |
| C82 | 1 | 57.33 | 40.33 | 0.42 |
| C83 | 1 | 57.33 | 40.34 | 0.42 |
| C91 | 1 | 58.96 | 38.70 | 0.40 |
| C92 | 1 | 59.07 | 38.60 | 0.40 |
| C93 | 1 | 59.21 | 38.46 | 0.40 |

Initial $SO_4^{2-}$ conc. = 97.666 mg/L
Molar mass of $SO_4^{2-}$ = 96.06 g/mol

***Appendix C.4: Adsorption data for 18_ALSFH***

| Samples | Dilution factor | Diluted conc. (mg/L) | Amount sorbed (mg/L) | Amount sorbed (mM) |
|---|---|---|---|---|
| D31 | 1 | 8.54 | 89.40 | 0.93 |
| D32 | 1 | 8.32 | 89.62 | 0.93 |
| D33 | 1 | 8.37 | 89.57 | 0.93 |
| D41 | 1 | 25.45 | 72.49 | 0.75 |
| D42 | 1 | 25.52 | 72.42 | 0.75 |
| D43 | 1 | 25.37 | 72.57 | 0.76 |
| D51 | 1 | 34.29 | 63.65 | 0.66 |
| D52 | 1 | 34.24 | 63.70 | 0.66 |
| D53 | 1 | 34.25 | 63.69 | 0.66 |
| D61 | 1 | 53.46 | 44.48 | 0.46 |
| D62 | 1 | 52.40 | 45.54 | 0.47 |
| D63 | 1 | 52.13 | 45.81 | 0.48 |
| D71 | 1 | 69.96 | 27.98 | 0.29 |
| D72 | 1 | 69.76 | 28.18 | 0.29 |
| D73 | 1 | 69.65 | 28.29 | 0.29 |
| D81 | 1 | 78.44 | 19.50 | 0.20 |
| D82 | 1 | 79.14 | 18.80 | 0.20 |
| D83 | 1 | 79.01 | 18.93 | 0.20 |
| D91 | 1 | 81.40 | 16.54 | 0.17 |
| D92 | 1 | 81.49 | 16.45 | 0.17 |
| D93 | 1 | 81.86 | 16.08 | 0.17 |

Initial $SO_4^{2-}$ conc. = 97.938 mg/L
Molar mass of $SO_4^{2-}$ = 96.06 g/mol

***Appendix C.5: Adsorption data for 24_ALSFH***

| Samples | Dilution factor | Diluted conc. (mg/L) | Amount sorbed (mg/L) | Amount sorbed (mM) |
|---|---|---|---|---|
| E31 | 1 | 2.67 | 93.50 | 0.97 |
| E32 | 1 | 2.43 | 93.74 | 0.98 |
| E33 | 1 | 2.61 | 93.56 | 0.97 |
| E41 | 1 | 9.27 | 86.90 | 0.90 |
| E42 | 1 | 9.65 | 86.52 | 0.90 |
| E43 | 1 | 9.64 | 86.53 | 0.90 |
| E51 | 1 | 22.97 | 73.20 | 0.76 |
| E52 | 1 | 21.44 | 74.73 | 0.78 |
| E53 | 1 | 21.56 | 74.61 | 0.78 |
| E61 | 1 | 41.55 | 54.62 | 0.57 |
| E62 | 1 | 42.30 | 53.88 | 0.56 |
| E63 | 1 | 44.41 | 51.76 | 0.54 |
| E71 | 1 | 62.59 | 33.58 | 0.35 |
| E72 | 1 | 61.60 | 34.57 | 0.36 |
| E73 | 1 | 60.70 | 35.47 | 0.37 |
| E81 | 1 | 71.18 | 24.99 | 0.26 |
| E82 | 1 | 69.14 | 27.03 | 0.28 |
| E83 | 1 | 70.15 | 26.02 | 0.27 |
| E91 | 1 | 73.73 | 22.45 | 0.23 |
| E92 | 1 | 72.65 | 23.52 | 0.24 |
| E93 | 1 | 77.95 | 18.22 | 0.19 |

Initial $SO_4^{2-}$ conc. = 96.171 mg/L
Molar mass of $SO_4^{2-}$ = 96.06 g/mol

## Appendix D: Multi-Point BET plots for synthesized Fh samples

### *Appendix D.1: Multi-Point BET plot for 0_ALSFH*

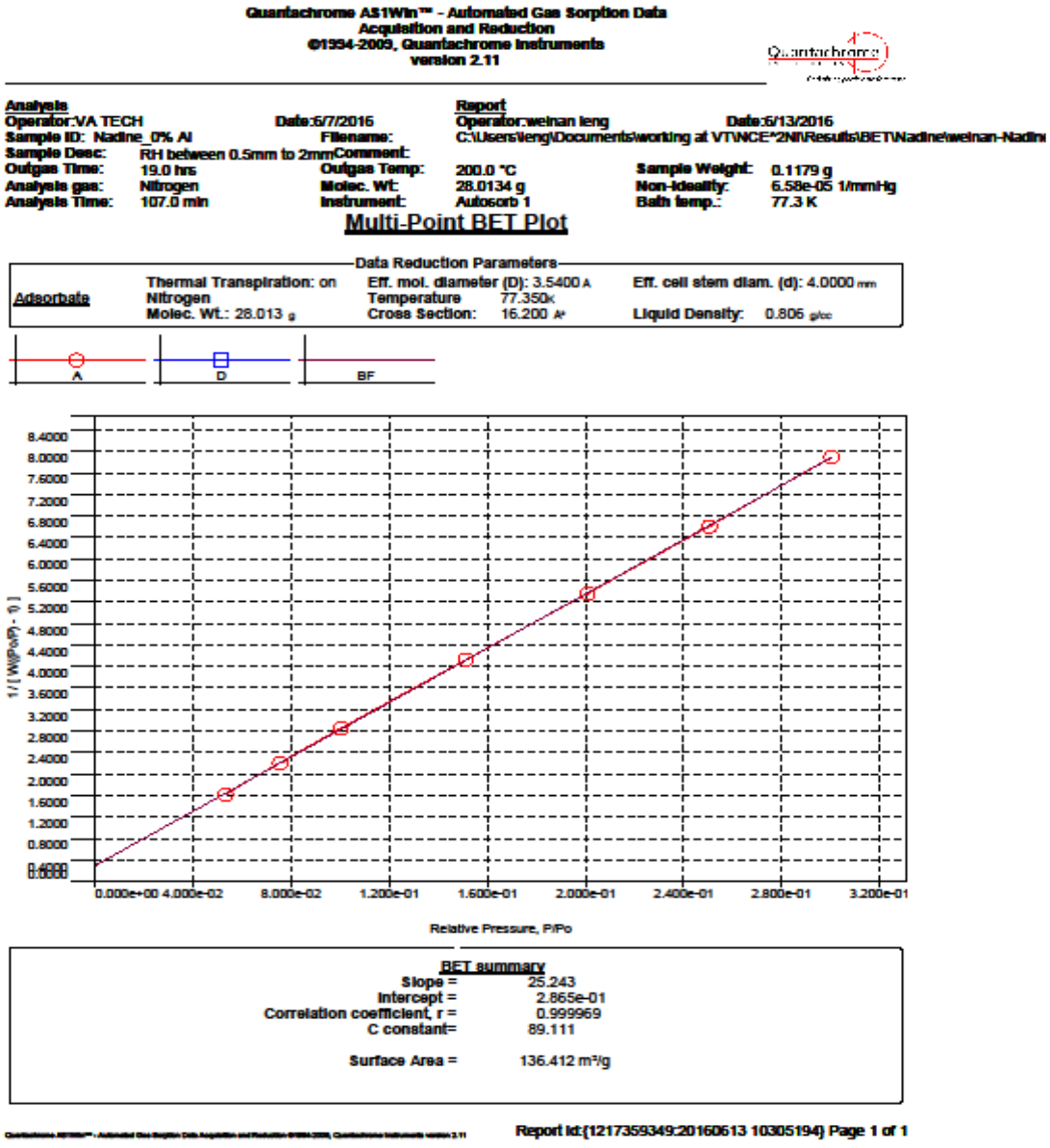

*Appendix D.2: Multi-Point BET plot for 6_ALSFH*

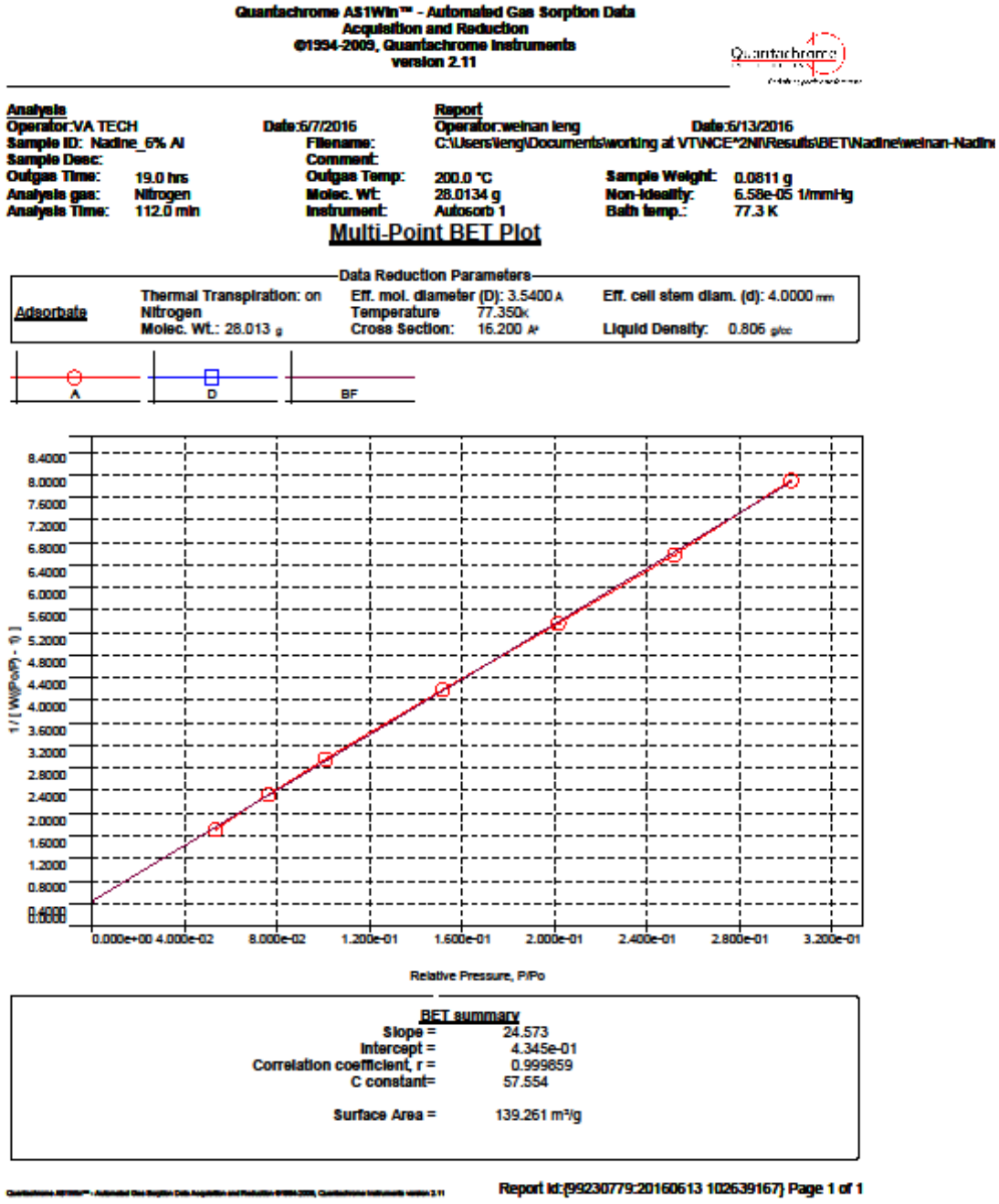

Quantachrome AS1Win™ - Automated Gas Sorption Data Acquisition and Reduction
©1994-2009, Quantachrome Instruments
version 2.11

Analysis Operator:VA TECH
Sample ID: Nadine_6% Al
Sample Desc:
Outgas Time: 19.0 hrs
Analysis gas: Nitrogen
Analysis Time: 112.0 min

Date:6/7/2016
Filename:
Comment:
Outgas Temp: 200.0 °C
Molec. Wt: 28.0134 g
Instrument: Autosorb 1

Report Operator:weinan leng
Date:6/13/2016
C:\Users\leng\Documents\working at VT\NCE^2NI\Results\BET\Nadine\weinan-Nadine

Sample Weight: 0.0811 g
Non-Ideality: 6.58e-05 1/mmHg
Bath temp.: 77.3 K

Multi-Point BET Plot

Data Reduction Parameters

Adsorbate: Nitrogen
Molec. Wt.: 28.013 g
Thermal Transpiration: on
Temperature 77.350K
Cross Section: 16.200 A²
Eff. mol. diameter (D): 3.5400 A
Eff. cell stem diam. (d): 4.0000 mm
Liquid Density: 0.806 g/cc

A D BF

1 / [ W(Po/P) - 1) ]

8.4000 8.0000 7.6000 7.2000 6.8000 6.4000 6.0000 5.6000 5.2000 4.8000 4.4000 4.0000 3.6000 3.2000 2.8000 2.4000 2.0000 1.6000 1.2000 0.8000

0.000e+00 4.000e-02 8.000e-02 1.200e-01 1.600e-01 2.000e-01 2.400e-01 2.800e-01 3.200e-01

Relative Pressure, P/Po

BET summary

| | |
|---|---|
| Slope = | 24.573 |
| Intercept = | 4.345e-01 |
| Correlation coefficient, r = | 0.999659 |
| C constant= | 57.554 |
| Surface Area = | 139.261 m²/g |

Report Id:{99230779:20160613 102639167} Page 1 of 1

*Appendix D.3: Multi-Point BET plot for 12_ALSFH*

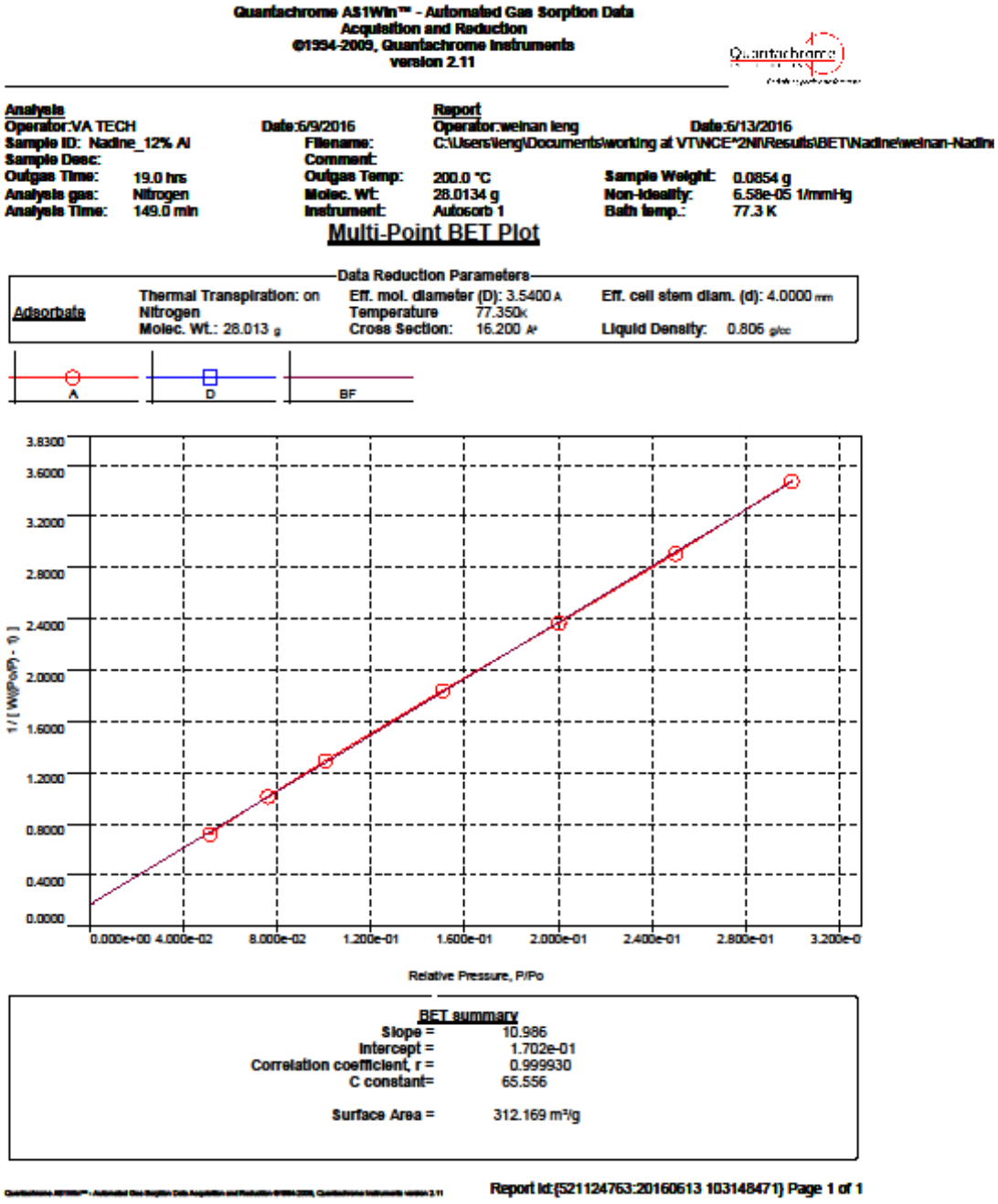

*Appendix D.4: Multi-Point BET plot for 18_ALSFH*

**Quantachrome AS1Win™ - Automated Gas Sorption Data Acquisition and Reduction**
**©1994-2009, Quantachrome Instruments**
**version 2.11**

Quantachrome

**Analysis**
Operator:VA TECH
Sample ID: Nadine_18% Al
Sample Desc:
Outgas Time: 19.0 hrs
Analysis gas: Nitrogen
Analysis Time: 136.0 min
Date:6/10/2016

**Report**
Operator:weinan leng
Date:6/13/2016
Filename: C:\Users\leng\Documents\working at VT\NCE^2NI\Results\BET\Nadine\weinan-Nadine
Comment:
Outgas Temp: 200.0 °C
Molec. Wt: 28.0134 g
Instrument: Autosorb 1
Sample Weight: 0.089 g
Non-Ideality: 6.58e-05 1/mmHg
Bath temp.: 77.3 K

## Multi-Point BET Plot

**Data Reduction Parameters**

Adsorbate: Nitrogen
Molec. Wt.: 28.013 g
Thermal Transpiration: on
Temperature 77.350K
Eff. mol. diameter (D): 3.5400 A
Cross Section: 16.200 A²
Eff. cell stem diam. (d): 4.0000 mm
Liquid Density: 0.806 g/cc

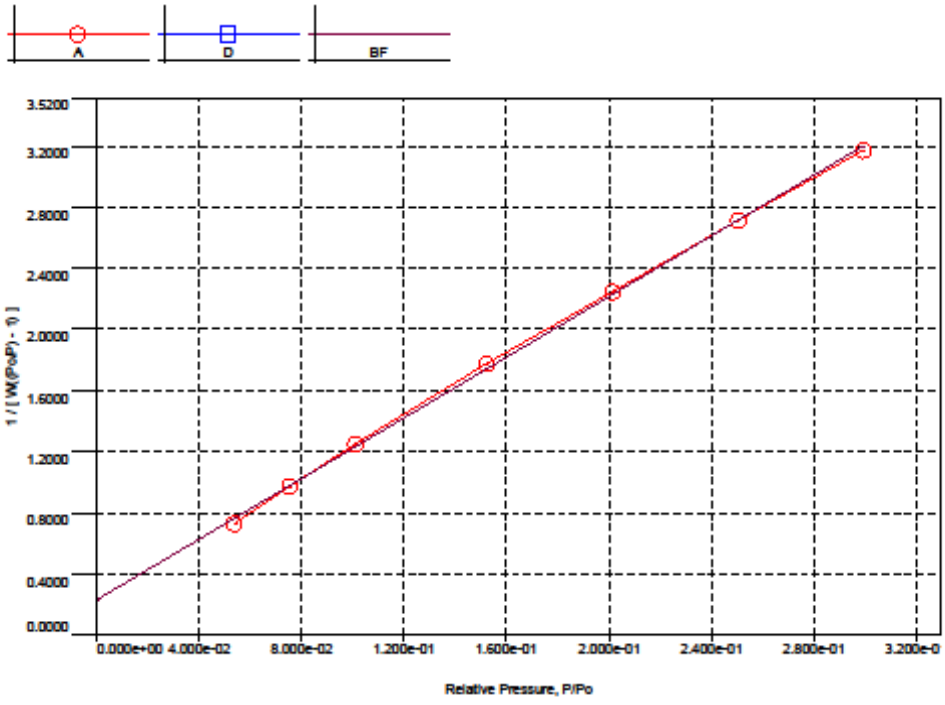


**BET summary**

| | |
|---|---|
| Slope = | 9.921 |
| Intercept = | 2.277e-01 |
| Correlation coefficient, r = | 0.999601 |
| C constant= | 44.572 |
| Surface Area = | 343.155 m²/g |

*Appendix D.5: Multi-Point BET plot for 24_ALSFH*

**Quantachrome AS1Win™ - Automated Gas Sorption Data Acquisition and Reduction**
**©1994-2009, Quantachrome Instruments**
**version 2.11**

Quantachrome

**Analysis**
Operator:VA TECH
Sample ID: Nadine_24% Al
Sample Desc:
Outgas Time: 7.0 hrs
Analysis gas: Nitrogen
Analysis Time: 132.0 min
Date:6/11/2016
Filename:
Comment:
Outgas Temp: 200.0 °C
Molec. Wt: 28.0134 g
Instrument: Autosorb 1

**Report**
Operator:weinan leng
Date:6/13/2016
C:\Users\leng\Documents\working at VT\NCE^2NI\Results\BET\Nadine\weinan-Nadine
Sample Weight: 0.0786 g
Non-Ideality: 6.58e-05 1/mmHg
Bath temp.: 77.3 K

## Multi-Point BET Plot

**Data Reduction Parameters**

Adsorbate: Nitrogen
Molec. Wt.: 28.013 g
Thermal Transpiration: on
Eff. mol. diameter (D): 3.5400 A
Temperature 77.350K
Cross Section: 16.200 A²
Eff. cell stem diam. (d): 4.0000 mm
Liquid Density: 0.806 g/cc

A D BF

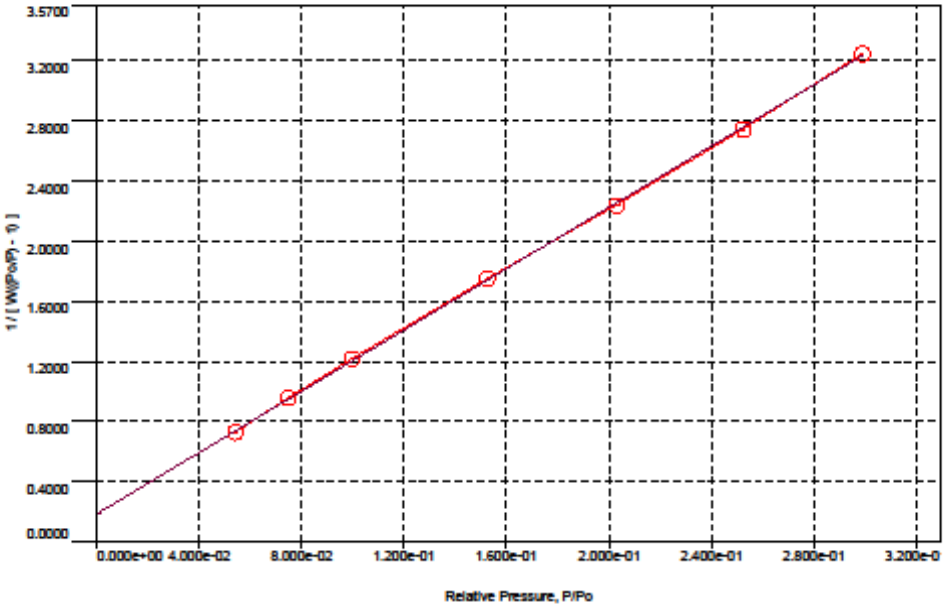


**BET summary**

| | |
|---|---|
| Slope = | 10.171 |
| Intercept = | 1.853e-01 |
| Correlation coefficient, r = | 0.999898 |
| C constant= | 55.880 |
| Surface Area = | 336.254 m²/g |

## Appendix E: Determination of Mineral Particle Dimensions

### *Appendix E.1: Unaged Samples*

| Sample | Length (nm) | Width(nm) | Aspect ratio | | |
|---|---|---|---|---|---|
| 0_ALSFH | 588.29 | 19.9 | 29.56 | | |
| | 570.77 | 16.84 | 33.89 | | |
| | 645.08 | 17.27 | 37.35 | Average = | 32.74 |
| | 676.18 | 21.89 | 30.89 | S.D = | ± 3.66 |
| | 253.66 | 6.99 | 36.29 | 99.9 % C.I = | 4.92 |
| | 422.29 | 14.84 | 28.46 | | |
| 6_ALSFH | 208.71 | 28.75 | 7.26 | | |
| | 214.09 | 26.72 | 8.01 | | |
| | 216.06 | 38.53 | 5.61 | Average = | 8.39 |
| | 137.19 | 17.83 | 7.69 | S.D = | ± 1.88 |
| | 208.85 | 24.33 | 8.58 | 99.9 % C.I = | 2.33 |
| | 275.61 | 25.02 | 11.02 | | |
| | 187.69 | 17.83 | 10.53 | | |
| 12_ALSFH | 291.41 | 33.83 | 8.61 | | |
| | 198.83 | 31.67 | 6.28 | | |
| | 237.09 | 35.46 | 6.69 | Average = | 8.33 |
| | 208.14 | 23.92 | 8.70 | S.D = | ± 2.08 |
| | 236.16 | 23.51 | 10.05 | 99.9 % C.I = | 1.71 |
| | 169.02 | 28.75 | 5.88 | | |
| | 249.01 | 22.23 | 11.20 | | |
| | 238.66 | 21.89 | 10.90 | | |
| | 226.81 | 37.79 | 6.00 | | |
| | 226.67 | 24.33 | 9.32 | | |
| | 276.47 | 40.05 | 6.90 | | |
| | 204.92 | 17.27 | 11.87 | | |
| | 158.07 | 26.72 | 5.92 | | |
| | 246.13 | 26.54 | 9.27 | | |
| | 145.8 | 23.82 | 6.12 | | |
| | 170.53 | 17.69 | 9.64 | | |

| | | | | | |
|---|---|---|---|---|---|
| 18_ALSFH | 185.78 | 29.09 | 6.39 | | |
| | 191.09 | 27.71 | 6.90 | Average = | 7.52 |
| | 200.68 | 28.75 | 6.98 | S.D = | ± 1.35 |
| | 238.86 | 24.33 | 9.82 | 99.9 % C.I = | 1.98 |
| | 153.77 | 20.39 | 7.54 | | |

***Appendix E.2: Aged Samples***

| Sample | Length (nm) | Width (nm) | Aspect ratio | | |
|---|---|---|---|---|---|
| 0_ALSFH | 261.13 | 19.03 | 13.72 | | |
| | 485.45 | 23.82 | 20.38 | Average = | 19.45 |
| | 337.6 | 17.69 | 19.08 | S.D = | ± 7.25 |
| | 246.93 | 19.9 | 12.41 | 99.9 % C.I = | 7.54 |
| | 335.57 | 25.79 | 13.01 | | |
| | 325.83 | 18.77 | 17.36 | | |
| | 287.93 | 14.16 | 20.33 | | |
| | 374.34 | 9.89 | 37.85 | | |
| | 427.94 | 19.9 | 21.50 | | |
| | 385.03 | 20.39 | 18.88 | | |
| 6_ALSFH | 147.04 | 18.9 | 7.78 | | |
| | 134.64 | 21.89 | 6.15 | | |
| | 142.96 | 20.98 | 6.81 | Average = | 7.14 |
| | 121 | 26.7 | 4.53 | S.D = | ± 1.84 |
| | 160.72 | 15.95 | 10.08 | 99.9 % C.I = | 2.14 |
| | 114.43 | 22.12 | 5.17 | | |
| | 122.62 | 15.48 | 7.92 | | |
| | 121.2 | 13.99 | 8.66 | | |
| 12_ALSFH | 170.07 | 14.84 | 11.46 | | |
| | 183.26 | 11.28 | 16.25 | Average = | 9.51 |
| | 177.28 | 22.12 | 8.01 | S.D = | ± 2.77 |
| | 165.05 | 23.51 | 7.02 | 99.9 % C.I = | 2.75 |
| | 177.51 | 21.89 | 8.11 | | |
| | 208 | 26.54 | 7.84 | | |
| | 151.3 | 13.46 | 11.24 | | |
| | 191.02 | 17.69 | 10.80 | | |
| | 146.5 | 22.12 | 6.62 | | |
| | 135.69 | 15.64 | 8.68 | | |
| | 152.67 | 17.83 | 8.56 | | |

| | | | | | |
|---|---|---|---|---|---|
| 18_ALSFH | 170.66 | 22.77 | 7.49 | | |
| | 168.44 | 13.99 | 12.04 | | |
| | 139.48 | 16.84 | 8.28 | Average = | 9.85 |
| | 144.23 | 20.39 | 7.07 | S.D = | ± 3.87 |
| | 120.33 | 14.1 | 8.53 | 99.9 % C.I = | 3.83 |
| | 117.22 | 11.06 | 10.60 | | |
| | 182 | 9.12 | 19.96 | | |
| | 102.91 | 20.39 | 5.05 | | |
| | 216.63 | 20.39 | 10.62 | | |
| | 151.51 | 15.64 | 9.69 | | |
| | 218.34 | 24.33 | 8.97 | | |
| 24_ALSFH | 106.34 | 18.9 | 5.63 | | |
| | 128.75 | 13.45 | 9.57 | | |
| | 105.51 | 20.08 | 5.25 | Average = | 6.91 |
| | 106.76 | 18.9 | 5.65 | S.D = | ± 1.58 |
| | 102.46 | 15.64 | 6.55 | 99.9 % C.I = | 1.65 |
| | 113.34 | 17.83 | 6.36 | | |
| | 109.11 | 15.48 | 7.05 | | |
| | 106.99 | 11.9 | 8.99 | | |
| | 85.89 | 15.64 | 5.49 | | |
| | 120.92 | 14.16 | 8.54 | | |

## Appendix F: EDX Spectra of ALSFH Samples Aged at 90° C for 48 h

### *Appendix F.1: EDX spectrum for 0_ALSFH*

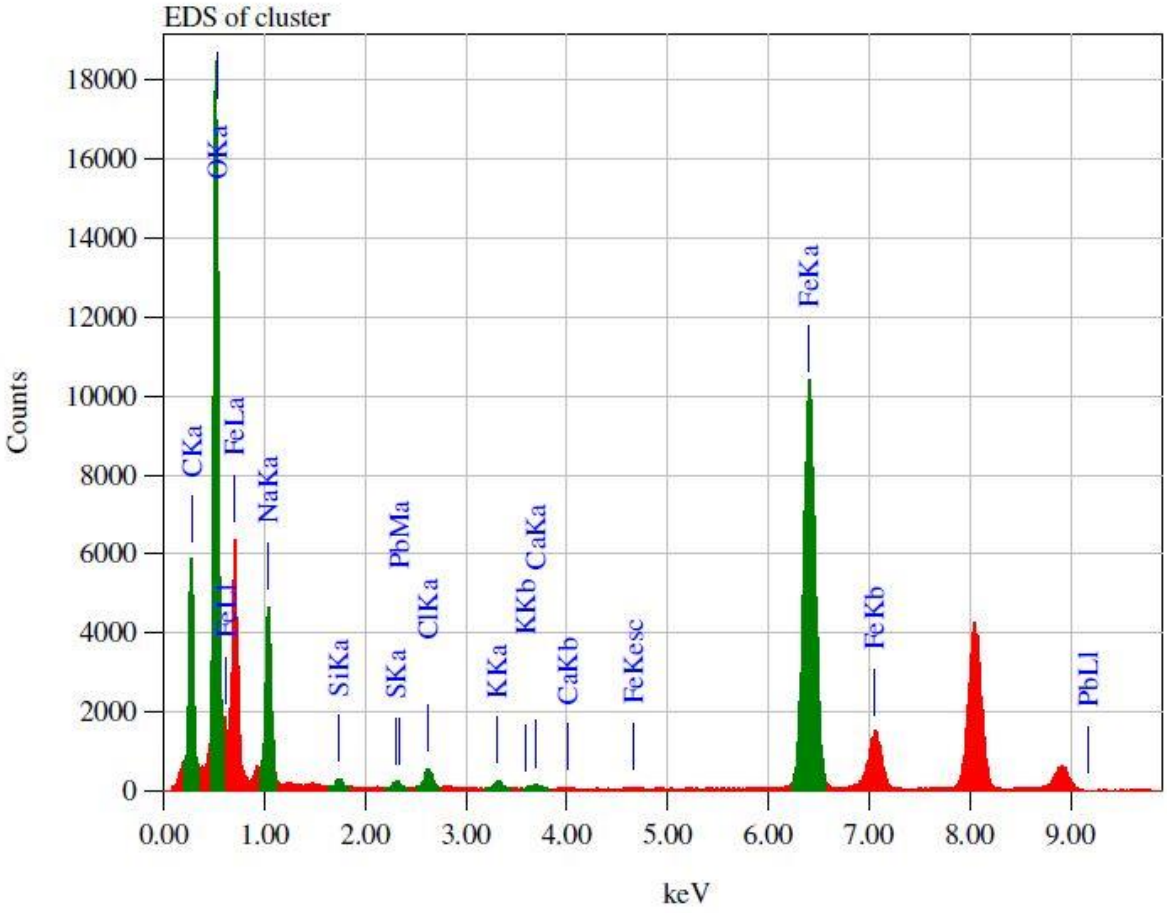

***Appendix F.2: EDX spectrum for 6_ALSFH***

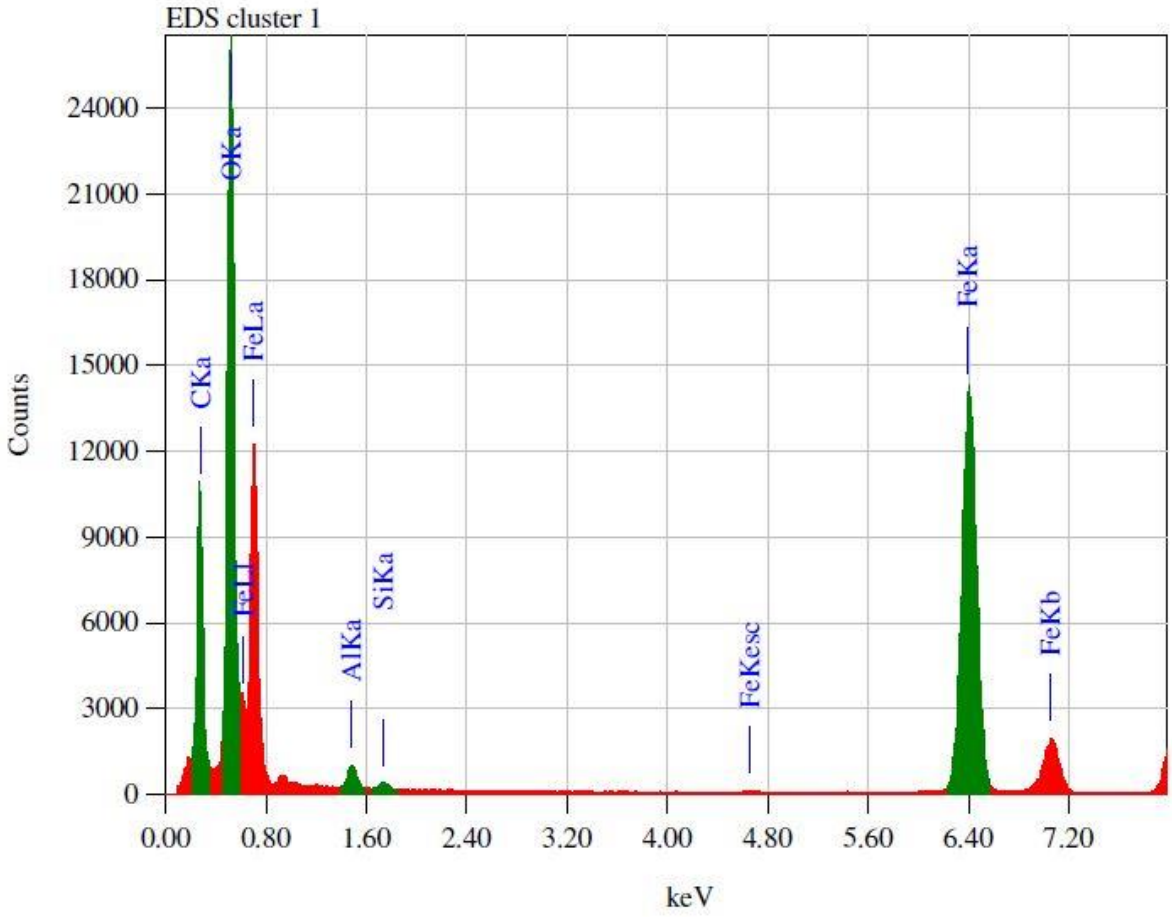

***Appendix F.3: EDX spectrum for 12_ALSFH***

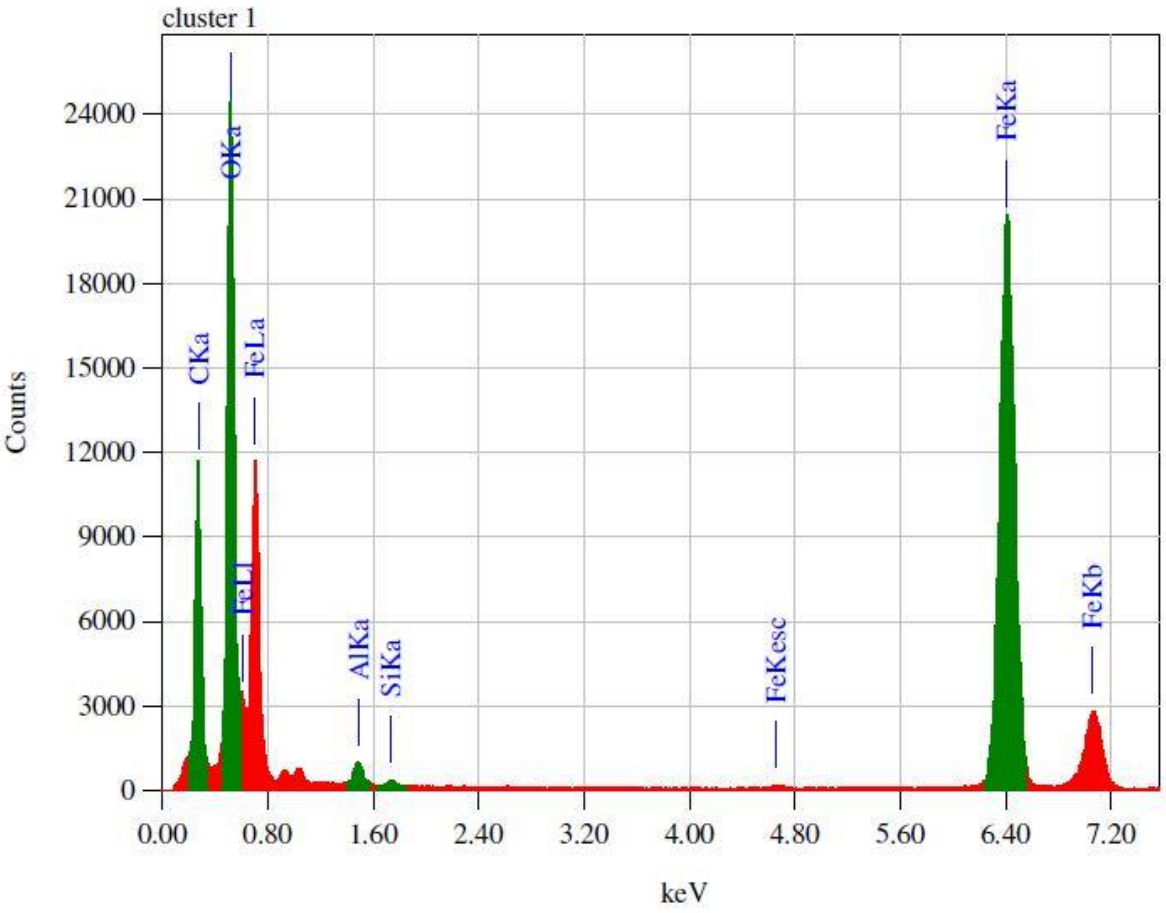

***Appendix F.4: EDX spectrum for 18_ALSFH***

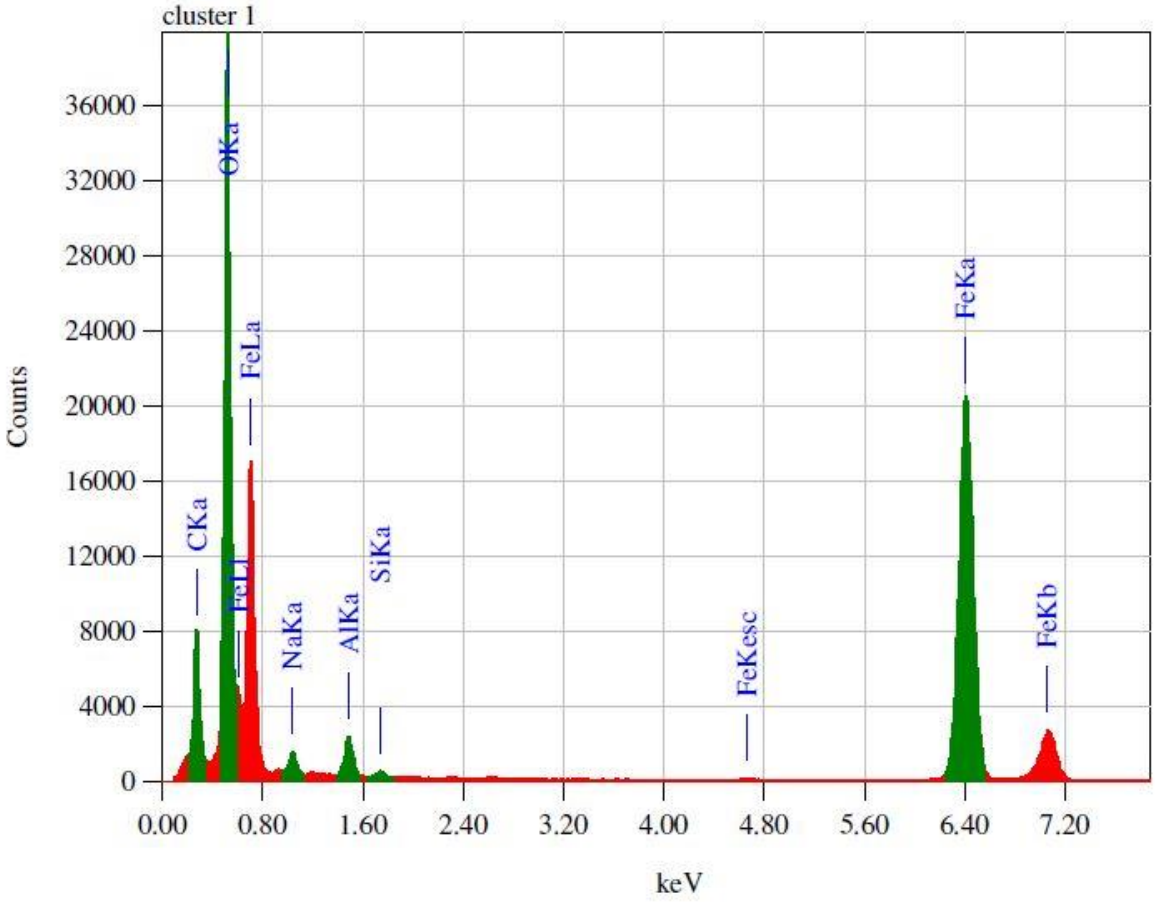

***Appendix F.5: EDX spectrum for 24_ALSFH***